INVESTIGATING LESIONS IN THE OPTIC CHIASM OF A MULTIPLE SCLEROSIS MODEL BY QUANTITATIVE MAGNETIC RESONANCE IMAGING

BY

Annie Kim

A Thesis submitted to the Faculty of Graduate Studies of

The University of Manitoba

in partial fulfillment of the requirements of the degree of

MASTER OF SCIENCE

Department of Pharmacology and Therapeutics

University of Manitoba

Winnipeg

THE UNIVERSITY OF MANITOBA

FACULTY OF GRADUATE STUDIES

*****

COPYRIGHT PERMISSION

Investigating Lesions in the Optic Chiasm of a Multiple Sclerosis Model by Quantitative Magnetic Resonance Imaging

By

Annie Kim

A Thesis/Practicum submitted to the Faculty of Graduate Studies of The University of Manitoba in partial fulfillment of the requirement of the degree

Of

Master of Science

ABSTRACT

Conventional magnetic resonance imaging cannot provide pathological specificity of white matter disease (e.g., experimental autoimmune disease, EAE). Diffusion-weighted imaging (DWI), an advanced imaging technique, was performed to test putative markers in the optic chiasm of myelin oligodendrocyte glycoprotein peptide 35-55 immunized EAE mice (N=39). Apparent diffusion coefficients in longitudinal ($ADC_{\parallel}$) and perpendicular ($ADC_{\perp}$) directions of the axonal tracts, in addition to the mean ADCs and anisotropies were calculated and compared with histology. Mice, including wild type (N=6) and sham controls (N=3) were imaged at pre-disease and at targeted onset and peak disease. ADCs in the optic chiasm increased with EAE suggesting myelin damage, mixed inflammation and edema, which were confirmed with histology. There was no reduced $ADC_{\parallel}$ despite the occurrence of early axonal damage. Axon crossings might have contributed to the low and consistent anisotropies. These DWI results suggest a means for non-invasive pathological specificity.

ACKNOWLEDGEMENTS

The completion of this thesis could not have been achieved if it were not for my support system, to which I am forever indebted. From supervisor and affiliates to family and friends, I am greatly thankful for all of your unconditional encouragement and advice during the good, the bad and the ugly in obtaining my Master of Science degree.

To my supervisor, mentor and friend, Dr. Melanie Martin, thank you for providing this opportunity to engage in real science. There are not enough words to describe my gratitude for your full support, guidance, trust in my independence and patience throughout the course of my studies. Further thanks to:

- Dr. Richard Buist for making my MRI experiments possible, and in providing your expertise on NMRI.
- Dr. Marc Del Bigio for making my histology experiments possible, and in providing your dedication and your excellent insights to my thesis.
- Mr. Randy Summers for providing your expertise in statistics and helping me make sense of my results.
- Dr. Don Smyth and Dr. Chris Anderson for taking the time to help shape my project and in making my committee meetings pleasurable.
- Dr. Angela Schellenberg for taking the time to train me and provide your experience with my animal experiments.
- Dr. Fiona Parkinson for allowing me access to your sterile fume-hood.
- Mr. Jonathan Thiessen for your time and assistance in specializing MATLAB codes for my image analysis.

To mom and dad, thank you for moving what seems like heaven and earth in supporting my education and always believing in me. To Hans, Jo, Michelle, Mary, Krista and Val, I made it because of you guys!

This thesis is dedicated to umma and appa.

Without your love and constant faith I would have never come this far.

Thank you for setting the perfect example of perseverance and self-control.

I am blessed to have both of you in my life.

TABLE OF CONTENTS

LIST OF TABLES

LIST OF FIGURES

LIST OF APPENDICES

LIST OF ABBREVIATIONS AND SYMBOLS

3V	third ventricle
γ	gyromagnetic ratio
θ	flip angle
τ	duration of the RF pulse
ν_o	cyclic frequency
ω_o	angular frequency
ω_1	angular frequency describing the rotation of the applied RF pulse
ACC	Animal Care Committee
ADC	apparent diffusion coefficient
$ADC_{\|\|}$	apparent diffusion coefficient in the longitudinal direction
$ADC_{\perp}$	apparent diffusion coefficient in the perpendicular direction
ADC_{mean}	mean apparent diffusion coefficient
ADC_x	apparent diffusion coefficient in the x-direction
ADC_y	apparent diffusion coefficient in the y-direction
ADC_z	apparent diffusion coefficient in the z-direction and, approximation for $ADC_{\|\|}$
ANOVA	analysis of variance
APC	antigen presenting cell
b	diffusion weighting factor
B_o	external magnetic field
B_1	magnetic component of the applied RF pulse
BBB	blood brain barrier

CAM	cellular adhesion molecule
CFA	complete Freund's adjuvant
CNS	central nervous system
CSF	cerebral spinal fluid
D	self-diffusion coefficient
DTH	delayed-type hypersensitivity
DTI	diffusion tensor imaging
DWI	diffusion-weighted imaging
EAE	experimental autoimmune encephalomyelitis
EM	electron microscopy
FA	fractional anisotropy
FEG	frequency encoding gradient
FOV	field of view
G_x	magnetic field gradient in x-direction
G_y	magnetic field gradient in y-direction
G_z	magnetic field gradient in z-direction
^1H	hydrogen nuclei
HE	hematoxylin and eosin
HLA	human leukocyte antigen
I	intensity
I_o	initial intensity
IFN-γ	interferon-gamma
IL-1	interleukin-1

IL-2	interleukin-2
IL-7	interleukin-7
IL-12	interleukin-12
LV	lateral ventricle
M	magnetization vector
M_o	equilibrium magnetization
M_{xy}	transverse component of the magnetization vector
M_z	longitudinal component of the magnetization vector
MAG	myelin associated glycoprotein
MBP	myelin basic protein
MHC	major histocompatibility complex
MOG	myelin oligodendrocyte glycoprotein
MOG_{33-55}	myelin oligodendrocyte glycoprotein peptide segment 35-55
MRI	magnetic resonance imaging
MS	multiple sclerosis
NEX	number of excitations
NMR	nuclear magnetic resonance
ON	optic neuritis
OX	optic chiasm
PBS	phosphate buffer saline
PEG	phase encoding gradient
PLP	proteolipid protein
POI	point of interest

PPMS	primary progressive multiple sclerosis
PRMS	primary relapsing multiple sclerosis
PTX	pertussis toxin
RA	relative anisotropy
RF	radiofrequency
ROI	region of interest
RRMS	relapsing remitting multiple sclerosis
SC	solochrome cyanine
SE	spin echo
SEM	standard error of the mean
SNR	signal to noise ratio
SPMS	secondary progressive multiple sclerosis
SSG	slice select gradient
T1	'spin-lattice' relaxation time
T1W	T1-weighted
T2	'spin-spin' relaxation time
T2W	T2-weighted
TCR	T cell receptor
TE	echo time
Th1	type 1 helper T cell
Th2	type 2 helper T cell
TNF-α	tumor necrosis factor-α
TR	repetition time

VEP	visual evoked potential
WM	white matter

CHAPTER 1: Introduction

1.1 Multiple sclerosis

Multiple sclerosis (MS) is one of the leading chronic neurological disorders disabling young adults. It affects twice as many women as men. The current prevalence of MS cases worldwide is estimated to be 2.5 million [1], with conspicuous trends in regions of higher latitudes. These regions include the western hemisphere such as Canada, Northern United States, and Northern Europe. In Canada alone, the MS population is estimated to be 75,000 [2].

Although the pathoetiology of the disease is unknown, extensive studies consider MS to be an autoimmune disease. A T cell-mediated inflammatory immune response might initiate the precipitating events. MS, which literally means 'many scars', marks both the brain and the spine – the central nervous system (CNS). The primary target for such scars is the myelin sheath that normally insulates the underlying nerve fiber (axon). In efforts to counteract these attacks, the body attempts to repair the exposed regions by remyelination. However these attempts eventually succumb because MS also destroys the myelin synthesizing and axon supporting cells (i.e., oligodendrocytes) along with the myelin [1,3]. As a result of demyelination and remyelination, scar tissue (i.e., sclerosis/gliosis) also referred to as plaques impair electrical impulses. Plaques could cause signs and symptoms that compromise motor, autonomic and neurocognitive functions because electrical impulses normally travel to and from the brain [1,4].

The course of MS is unpredictable [5] and can include active episodes that decrease the quality of life and increase risks for complications. Pathological attributes

include inflammation, demyelination and possible axonal degeneration with restricted repair. At least two demyelinating lesions (separated in time and space) are prerequisites to clinically define MS as a neurological disorder. The disease heterogeneity extends to lesion type, site and quantity as well as signs, symptoms and the classification of the disease itself. For all these reasons, pre-clinical studies that utilize appropriate MS models are further necessitated.

1.1.1 Clinical course of MS

MS can be difficult to diagnose because there are no distinct features that are specific to the disease. The course of the disease is characterized by episodes (or relapses after initial onset) with full or incomplete recovery (or remission) and chronic progression. This classifies the disease course into different categories: relapsing-remitting MS (RRMS), secondary progressive MS (SPMS), primary progressive MS (PPMS) and progressive relapsing MS (PRMS). RRMS is the most common form at onset (approximately 80 to 85%), which includes episodes that can fully recover [1,6-8]. However, the extent of remission decreases with time and approximately 30 to 40% of RRMS patients progress further to SPMS [9]. There are no full remissions in SPMS and relapses usually get worse. In PPMS there is gradual worsening of disease from onset, and less periodic plateaus and remissions compared to RRMS. PRMS is also progressive from onset but acute relapses are more distinct than in PPMS. In some cases, there might be incomplete remission. The time between relapses that is marked by gradual worsening of the disease makes PRMS distinct from RRMS [6].

1.1.2 Common symptoms and signs of MS

Despite the lack of clinical aspects that are specific for MS, there are a number of common presenting symptoms and signs. These include visual and motor impairment(s), paresthesias (i.e., abnormal sensation of tingling, numbness, prickling and burning) and general weakness. Initial disruptions can also include neurogenic bladder and bowel dysfunctions, sexual dysfunction, depression, vertigo, Lhermitte's sign (i.e., tingling sensation along the spine brought on by neck movements), fatigue and worsening episodes with increasing body temperature [10-12]. The visual impairment can involve either one eye or both eyes, whereas motor impairments can include gait and limb ataxia (i.e., loss of coordination). Additional common clinical features of MS include female predominance and early onset (i.e., between ages 15 and 50 years) of the disease, as well as its common relapsing and remitting nature [12].

1.1.3 Optic neuritis

Optic neuritis (ON) is a general term that refers to any inflammation that affects the optic nerves and usually includes the enlargement of the nerve and surrounding sheath [13-15]. Various visual disturbances possibly from inflammation (that can be associated with demyelination) are common amongst afflicted individuals [13]. Movement of the eyeball can aggravate pain that usually affects only one eye [13,16]. This condition can quickly involve severe vision loss but patients often recover [17]. When ON occurs on its own, it is considered a clinically isolated syndrome (i.e., monosymptomatic). However, ON often represents a manifestation of MS [18]. MS

patients frequently experience ON at some time in their disease course [13,18], and 40-70% of clinically isolated ON cases progress to MS [19].

1.1.4 MS diagnosis

MS diagnosis relies on lesion presentation that is disseminated in time and space (i.e., by at least three months in different regions of the CNS). The diagnostic criteria include a number of laboratory investigations rather than one single test. This is because no single disease feature distinctively defines MS and no one test is completely reliable for disease identification. A diagnostic process can involve studies with magnetic resonance imaging (MRI), cerebral spinal fluid (CSF) analysis and evoked potential testing [20].

Although evoked potential testing and CSF analysis are less common since the advent of MRI, they are still useful for differential diagnosis. Evoked potentials might demonstrate conduction changes relative to demyelination in the sensory (visual, brainstem auditory and somatosensory) pathway and help locate subclinical lesions. Examination of the CSF might provide information about intrathecal inflammation by the presence of oligoclonal bands and/or elevated levels of immunoglobulin G [21]. Neither are MS specific [10].

The testing of visual evoked potential (VEP) is considered the most useful of the evoked potential tests. This is because lesions in the optic nerve that are difficult to detect with MRI can be located with VEP testing [10]. The sensitivity of VEP testing might also extend to clinically silent lesions [22,23]. VEP testing visually stimulates the patient. For example, an alternating black and white checkerboard pattern (e.g.,

alternating at a frequency of 2Hz) can provide visual stimulation and allow measurements of the electrical impulses of the visual afferent pathway. This pathway begins in the retina and extends to the optic nerve, chiasm, tract, radiations and visual cortex. The response at the cortex is measured using recording electrodes that are affixed extracranially at the occiput [15]. A delay in the latency of VEP signals and the decrease in VEP intensities are linked to the loss of myelin and axon integrity, respectively [24,25].

One aspect of MRI that is advantageous over other assessments is its ability to provide anatomical dissemination of lesions (including some that are clinically silent) [1,8,10]. If a new lesion is found with MRI within three months following a clinically isolated syndrome, an early diagnosis of MS is possible. While MRI is one of the most useful methods for MS diagnosis [20], current conventional techniques only offer lesion sensitivity, whereas advanced imaging protocols offer potential pathological specificity (*Chapter 3*).

1.1.5 Immunology of MS

The exact cause of MS is not clear but the autoimmune theory still remains with particular emphasis on the role of T helper cells with CD4 cell-surface molecules (i.e., CD4+ T cells) [26,27]. Peripheral activation of autoreactive immune T cells with antigen receptors occurs before they can traverse the blood brain barrier (BBB) [28,29]. By the process of transmigration, activated T cells enter the CNS. The CNS normally does not sustain T cells but if they undergo reactivation they can orchestrate an inflammatory cascade (i.e., epitope spreading and the clonal expansion of T cells). The initial

activation in MS might result from a combination of genetic susceptibility and environmental factors [26,28,29], which include the role of infectious agents.

In MS, susceptible genes include the area of the major histocompatibility complex (MHC) [30,31]. The MHC resides on chromosome 6p21 and is divided into class I and class II sub-regions [32]. While the specific allelic associations remain elusive, one consistent finding is the association of the human leukocyte antigen (HLA) class II allele, HLA-DR2, with MS [31,33-35]. Different combinations of haplotypes can vary the disease susceptibility and further complicates the etiology of MS [32]. Recent studies also consider non-MHC associations with interleukin-7 (IL-7) receptor alpha [36,37], interleukin-2 (IL-2) receptor alpha [38] and kinesin family member 1B genes [39].

Possible environmental contributors of MS include ultraviolet radiation and hygiene. Insufficient exposure to ultraviolet radiation, a prerequisite for vitamin D biosynthesis, might explain the vitamin D deficiency in most MS patients. The greater prevalence rates in higher latitudes and over-expression of vitamin D receptor gene in MS patients supports this hypothesis [40]. In developed countries, late or reduced exposure to childhood infections is also a plausible environmental stimulus and is the basis for the yet unproven hygiene hypothesis [4]. Perhaps the more favoured environmental triggers (molecular mimicry and bystander activation) are two mechanisms that theorize the infectious induction of MS.

Post-infection, molecular mimicry can activate autoreactive T cells and lead an attack on both the invading pathogen and the host tissue. Molecular mimicry is the recognition of similar amino acid sequences between the host antigens and the foreign agents. Following recognition, molecular mimicry might lead to cross-reactivity and

activation of autoreactive immune cells (T cells). The similar homologies between myelin basic protein (MBP) and several viral pathogens (e.g., measles, influenza virus, adenovirus, herpes virus and Epstein-Barr virus) provide the evidence for this mechanism [41]. Some studies also implicate Chlamydia pneumonia as a possible infectious agent [42,43].

The bystander activation of autoreactive T cells involves a nonspecific inflammatory process during infection. Two possible mechanisms for T cell activation include:

A) Inflammatory cytokines and chemokines [44], superantigens [45] and Toll-like receptors [46] that are independent of T cell receptors (TCRs).

B) Class II MHC proteins on the surface of antigen presenting cells (APCs such as macrophages and CNS-resident glial cells) that carry the antigen for TCR recognition [47].

Following activation, there is localization and infiltration of lymphocytes. This involves chemoattraction, rolling adhesion, tight adhesion and transmigration. In addition to the activated T cells, activated macrophages and CNS-resident APCs such as astrocytes and microglia contribute to autoimmunity. Activated macrophages engulf pathogens and release pro-inflammatory (i.e., type 1 helper T cell, Th1) cytokines and chemokines. Microglia are resident macrophages of the brain and therefore provide the first line of immune defense (in the brain) by release of cytokines and growth-promoting factors. Cytokines and growth-promoting factors for endogenous remyelination can also be released by reactive astrocytes [1].

The release of cytokines and chemokines causes the up-regulation of adhesion molecules (e.g., cellular adhesion molecules (CAMs) including selectins) on the vessel wall. Within the post-capillary venule of the CNS, chemokines attract lymphocytes to the site of injury. Reduced shear stress facilitates the random contact between selectin ligands on the circulating T cells, and allows the rolling adhesion to the vessel wall. A tight adhesion requires the interaction of intracellular and vascular CAMs with counter-ligands, lymphocyte function-associated antigen-1 and very late antigen-4. Circulating T cells that express CAMs and their counter-ligands provide the firm adhesion necessary for transmigration through the endothelial cell layer [48,49]. The final step of transmigration (past the underlying basement membrane) depends on the production of metalloproteases such as matrix metalloproteinases. Matrix metalloproteinases cleave membrane components [50] and allow the T cell entry into the CNS.

Upon CNS entry, T cells require reactivation that occurs by recognition of the antigen present on the surface of the APC (e.g., microglia and astrocytes) [29]. TCRs can recognize a number of different antigens such as MBP, proteolipid protein (PLP), myelin oligodendrocyte glycoprotein (MOG) and myelin-associated glycoprotein (MAG) [51,52]. After T cell reactivation (i.e., T cells bind to antigen on local APCs), they release Th1 cytokines such as interleukin-1 (IL-1), interferon-γ (IFN-γ) and tumor necrosis factor-α (TNF-α). These activate monocytes and CNS-resident glial cells and further release neurotoxic components (i.e., nitric oxide, oxygen free-radicals etc), all of which contribute to myelin and axonal damage [53]. The pro-inflammatory cytokines can also activate the T cells to stimulate its clonal expansion with receptors for the same antigen and thereby contribute to the autoimmune inflammatory reaction of MS.

The autoimmune theory of MS favours the role of CD4+ T cells. While other immune cells (e.g., CD8+ T cells, macrophages, dendritic cells, neutrophils and B cells) might play a role [50,54,55], data from experimental autoimmune encephalomyelitis (EAE) studies support the involvement of CD4+ T cells [4,26,56]. EAE is an animal model of MS and is the focus of the subsequent section.

1.2 Experimental autoimmune encephalomyelitis

A number of animal models are possible to demonstrate the demyelinating pathology of MS. These models are inducible by myelin mutiny, chemical or viral induction or through an autoimmune process [57]. The Taiep rat and Shiverer (MBP mutants) [58-60], Rumpshaker and Jimpy dysmyelinated (PLP mutants) [61,62] and gene knockout (MAG) hypomyelinated mice [63] are all example models. Toxins such as lysolecithin (injections into the CNS), cuprizone (oral administration) or ethidium bromide can also cause demyelination [64-66]. Other demyelinating models result from Theiler's murine encephalomyelitis virus or Semliki Forest Virus infection [67,68]. However, the most common model is EAE [69].

There are many similar characteristics between EAE and MS. These resemblances reside in genetic susceptibility, environmental triggers, forms of disease, clinical presentation and pathology [70]. While the MHC II gene confers the most genetic susceptibility for EAE [71,72], other determinants (i.e., method of induction, strain and species) play a role in disease induction. Because these factors can differ, dissimilarities exist between EAE models and ultimately they recapitulate different aspects of MS [69,73]. For example, different myelin proteins (i.e., MBP [74], PLP [75-77], MOG [78], MAG [79,80]) or S-100 protein [81] can induce various forms of EAE. The inducible antigens for EAE are probable target antigens in MS and promote EAE by either molecular mimicry or bystander effect. As a result of antigen-strain-species selection there are different forms of EAE (e.g., chronic relapsing-remitting and non-remitting), which can differ in clinical presentation (*Section 1.2.2*) and pathology (*Section 2.3*). These differences are also true in human MS.

1.2.1 EAE induction with MOG

MOG is an antigen of the CNS [82] that belongs to the subclass type I of the immunoglobulin superfamily [83]. Its expression on the surface of the myelin sheath makes MOG a probable target antigen [84,85]. Although MOG makes up only 0.01-0.05% of myelin [86], it is the only antigen that results in both T cell mediated inflammation and demyelination [82]. MOG is more prevalent in the optic nerves compared to other parts of the CNS, which might explain the occurrences of ON and/or optic nerve lesions with EAE (following MOG_{35-55} induction) [70,87].

EAE induction with MOG requires either human or rodent MOG peptide segments 35-55 (MOG_{35-55}). EAE induction requires adjuvants for active immunization with MOG_{35-55}. The adjuvant that is selected can differ depending on the EAE model (i.e., antigen, strain and species used). Human MOG_{35-55} induction with complete Freund's adjuvant (CFA) and pertussis toxin (PTX) produce mild chronic, and severe chronic EAE [88]. Severe chronic EAE can also be induced in mice with rodent MOG_{35-55} [78,88,89].

The resulting immunopathological mechanisms via active immunization with MOG_{35-55} can parallel those present in MS. Both diseases include lesions with CD4+ T cells. CD4+ T cells can either express Th1 or type 2 helper T cell (Th2) response that release Th1 or Th2 cytokines, respectively. While the Th1 response is pro-inflammatory following the exposure to myelin components (e.g. MOG), Th2 cytokines are counteractive [90]. Both diseases depend on Th1 and Th2 responses (predominantly Th1), but MS does not require adjuvants (i.e., CFA and PTX) to potentiate cell-mediated immunity.

CFA is a common adjuvant that contains mycobacteria. It enhances MOG antigen exposure and thereby encourages an autoimmune response [91-93]. More specifically, CFA can mimic the pro-inflammatory mechanism of MS. After APC-antigen-T cell interaction, activated APCs release interleukin-12 (IL-12) [94]. IL-12 is a pro-inflammatory cytokine that is present within active MS lesions. In EAE, CFA increases IL-12 production and thereby engages CD4+ T cells in a Th1 response [95,96].

PTX, an excreted toxin of the Bortella pertussis bacterium, is an ancillary adjuvant for mouse EAE [97]. It provides adjuvant effects by both antibody and delayed-type hypersensitivity (DTH) responses. Because both Th1 and Th2 responses are involved, polyclonal and antigen-specific T cell activation, and IFN-γ production can be potentiated [98-101].

The addition of both CFA and PTX in the induction phase assists T cell migration through the BBB [102,103]. An antibody independent TNF-dependent mechanism can occur after MOG_{35-55} administration and thereby produce a demyelinating activity [89,104]. The DTH response in MS results from Th1 development that is IL-12 dependent. IL-12 allows Th1 cells to release inflammatory cytokines (e.g., IFN-γ and TNF-α) that provide DTH response, APC activation and further IL-12 production [105].

1.2.2 Clinical features of EAE

The clinical course, disease severity and presentation of EAE can all be heterogeneous much like MS. This is likely because of the different induction methods that produce different models of EAE. The different classifications of EAE include: acute, chronic progressive, chronic relapsing and chronic with delayed onset EAE [106].

Unlike MS, EAE can also be monophasic, such that animals completely recover from a single episode/onset of the disease [69]. Despite the difference in disease course compared to MS, monophasic EAE is still useful for study. For example, monophasic EAE is useful for pilot experiments that choose to investigate one particular aspect of EAE with novel techniques (e.g., measuring the diffusion in the optic chiasm).

Acute EAE typically causes fairly rapid fatality following immunization. There is rapid weight loss, hind limb weakness, eventual paralysis, incontinence, respiratory failure and possible death [107]. Chronic progressive EAE progresses more slowly. It typically occurs within two weeks of induction and can remain without recovery for up to 70 days [108]. Chronic relapsing models present signs of acute EAE that vary in severity and show recovery. These animals may experience hind limb weakness that progresses to paralysis and/or incontinence but gain complete remission of disease similar to RRMS. They may be free of all EAE signs for up to a month before their next relapse. Lastly, chronic EAE with delayed onset present with weight loss and general weakness within two weeks of immunization. Within one or two months neurological changes are apparent [106].

Depending on the site of lesion development, the presentation of EAE could involve any part of the CNS. Similar to MS, this might include the brain (i.e., periventricular inflammation), spinal cord (i.e., myelitis) and/or the optic nerve (i.e., ON). An ordinal scale that varies between studies, either by the number and/or definition of stages/scores can assess the clinical features of EAE (*Section 2.2*).

1.2.3 Pathological features of EAE

Although there are specific manifestations of EAE following the antigen-strain-species selection, EAE pathology is generally similar to MS. These parallels include T cell predominance, inflammation characterized by perivascular cuffing (i.e., accumulation of lymphocytes in the perivascular space), demyelination and axonal degeneration. The homing and invading process of lymphocytes into the CNS through the BBB also resembles the mechanism of MS (*Section 1.1.5*).

Demyelination is classified into primary and secondary subtypes. Primary demyelination is defined by the destruction of the myelin sheath that leaves the underlying axons bare. Secondary demyelination is first associated with axonal degeneration. The resulting loss of the myelin sheath occurs because maintenance is lost with decreased axonal integrity [109]. With disease progression axonal degeneration can also occur with primary demyelination [110].

Classical EAE models can exhibit T cell and macrophage mediated inflammation in the CNS of C57BL/6 mice. Previous histological examinations show typical perivascular infiltration of lymphocytes, secondary demyelination [78] and axonal damage [111,112]. A CD4+ T cell mediation [113] (i.e., T cell activation producing IFN-γ) is the likely mechanism in EAE pathogenesis [26,114,115]. As described for MS, autoreactive T cells might be activated in the periphery, and rely on the interaction of upregulated CAMs to traverse the BBB. Despite the major emphasis on CD4+ T cells, other immune cells (e.g., CD8+ T cells, microglia, astrocytes and B cells) might stimulate local T cells in EAE [54,116,117].

The histological characteristics of monophasic EAE induced in C57BL/6 mice with MOG_{35-55} and adjuvants include inflammation with associated local demyelination. Immune cells (i.e., T cells, B cells, macrophages and neutrophils) [118] can infiltrate the peripheral white matter (WM) of the spinal cord. Recent rodent EAE models report axonal damage with lesions in the optic nerves, ON and a greater severity of pathologies in the optic nerve relative to the spinal cord [111,119]. For all these reasons, the EAE immunization with MOG_{35-55} and adjuvants in this thesis anticipates lesion development in the optic chiasm.

1.3 The basics of magnetic resonance imaging

Magnetic resonance imaging (MRI) is a non-invasive method to obtain information about a biological system without ionizing radiation. The use of MRI is common practice to evaluate the immunopathological events of MS. Conventional MRI plays a role in disease diagnosis [20,120] and provides an endpoint measure in patient trials [121]. Small-animal studies also use MRI to provide anatomical images of the CNS (e.g., to study a disease course). Recent MRI techniques can potentially quantify anatomical abnormalities. Therefore, MRI is an invaluable tool to further define the pathoetiology of MS.

1.3.1 Nuclear magnetic resonance

MRI depends on the principles of nuclear magnetic resonance (NMR) in order to create images based on properties of the nuclei of atoms in tissue. NMR is a phenomenon that occurs only when nuclei that possess a magnetic dipole moment are within a strong external magnetic field (B_o). The magnetic dipole moment depends on the intrinsic spin properties of the nuclei [122]. Of the many nuclei that possess a magnetic dipole moment, proton (i.e., the nucleus of the hydrogen atom, ^1H) of water is most commonly studied. This is because water predominantly constitutes the mammalian composition and thus gives the strongest NMR signal [123].

The magnetic dipole moment property is analogous to bar magnets with north and south poles. At thermal equilibrium (without the application of B_o), the direction of magnetic dipole moment is random and there is no net magnetization (sum of magnetic

dipole moments from all nuclei). However, nuclei in the presence of B_o will have their magnetic moments align either parallel to (i.e., lower-energy state) or anti-parallel to (i.e., slightly higher-energy state) B_o [124]. The Boltzmann Distribution describes a slight bias towards more protons in the lower-energy state and provides a net (non-zero) magnetization (i.e., parallel to B_o when summed) [125]. This difference in energy contributes to the measurable signal in MRI.

1.3.2 Precession

A proton will also experience torque due to any applied magnetic field. This causes the proton to precess not only about its own axis (spin) but also about the axis of B_o. This motion is synonymous to the wobbling of a spinning top as a result of gravity. The precession occurs at an angular frequency (ω_o, measured as number of rotations per second about an axis of rotation) that is proportional to B_o. The Larmor equation mathematically defines the relationship between the magnitudes of ω_o and B_o to give the Larmor frequency [124,126]:

$$\omega_o = \gamma B_o$$

The gyromagnetic ratio (γ) is a constant that is nuclei specific.

For this thesis, the Larmor frequency was calculated using the gyromagnetic ratio of the ^1H nucleus, γ = 42.58 MHz/T [124]. All the experiments included in this thesis were conducted by application of an external 7.0 T magnetic field (i.e., B_o = 7.0 T). After the conversion of the angular frequency to cyclic frequency,

$$\nu_o = \omega_o / 2\pi$$

the Larmor frequency was ν_o =300 MHz .

1.3.3 Net magnetization vector

The net magnetization vector (**M**) is the sum of all the individual magnetic moments of nuclei and comprises of two components:

A) Longitudinal magnetization (M_z) in the z-direction (defined by B_o), and

B) Transverse magnetization (M_{xy}) in the x-y plane.

At equilibrium, M_z is at maximum and is parallel to B_o, whereas M_{xy} is zero and is orthogonal to B_o. This is because the randomized spins in the x-y plane have a canceling effect that set M_{xy} to zero [124]. This equilibrium magnetization (M_o) is proportional to the number of mobile protons per unit volume of a tissue (proton density). This proton density is tissue specific [126].

1.3.4 Radiofrequency pulse

An applied radiofrequency (RF) pulse is an electromagnetic wave within the RF range delivered for a short period of time. Protons within the B_o require an RF pulse to tip the net magnetization away from B_o towards the transverse plane. The RF pulse has its own magnetic component (B_1) that is weaker than B_o and applies torque onto the magnetization. Initially, if an RF pulse is applied, the magnetization is tipped away from the z-direction. The magnetic moments that make up the magnetization, which are originally aligned with B_o, precess in phase about B_o. Displacement of magnetization away from the longitudinal direction only occurs when the frequency of the RF pulse matches the Larmor frequency. A modification of the Larmor equation can describe the rotation of the magnetization away from the z-direction at an angular frequency,

$$\omega_1 = \gamma B_1$$

If ω_1 of the RF pulse is not at the Larmor frequency, the resonance between the two magnetic fields does not occur. Without resonance, there is no initial flip of magnetization, no precession of protons, and therefore there is no measurable NMR signal [126].

1.3.5 Flip angles

The flip angle (θ) is the angular rotation of the magnetization caused by the RF pulse. For instance, if a 90° pulse is applied, the magnetization rotates from the z-direction into the transverse plane, so that M_z goes to zero and M_{xy} has a magnitude of M_o. Although common flip angles are 90° and 180°, various angles can be used to create different types of tissue contrast in MRI. The strength (B_1) and duration (τ) of the RF pulse, with γ, determine the flip angle,

$$\theta = \gamma B_1 \tau$$

Given a constant B_1, the resulting flip angle will be larger with extended pulse time [124,126].

1.3.6 Relaxation

While the RF pulse application causes spin excitation, its cessation allows the system to return to equilibrium. Two processes occur simultaneously, but independently of each other to cause the return to equilibrium.

The spin-lattice relaxation time, known as T1, describes the exponential re-growth of M_z to M_o. The magnetic moments begin to realign with B_o and release energy to the local tissue (i.e., the lattice). This energy transfer is the 'spin-lattice' relaxation [125]. Energy transfer is most efficient (i.e., T1 is shortest) when the natural motional frequencies of protons are in sync with the Larmor frequency. The natural motional frequencies of protons are tissue specific and its difference from the Larmor frequency determines (the length of) the T1 relaxation time [126].

Just as M_z returns to equilibrium, M_{xy} decays exponentially to zero with a time constant of T2. T2 relaxation time is the 'spin-spin' relaxation because it describes the energy transfer between magnetic moments (spins). The 'spin-spin' relaxation is part of the phenomena that make the initial (after the RF cessation) in phase magnetic moments go out of phase (i.e., dephase) [126].

T1 is either greater than or equal to T2. In general, T1 is on the order of seconds or tenths of seconds, whereas T2 is often hundredths to tenths of seconds [124]. In the mouse brain at B_o = 7.0 T, T1 and T2 values are approximately 1500 ms and 40 ms, respectively [127].

1.4 MR image production

Whether MRI is applied in clinical or laboratory studies, the fundamentals are the same and involve B_o, RF pulses and some measurable nuclei. In laboratory studies, once the animal is in position within the magnetic bore, B_o aligns ^1H proton magnetic moments intrinsically existing within the animal. The application of RF pulse proceeds and displaces the magnetization into the transverse plane by a specified flip angle (*Section 1.3.5*). When the RF pulse ceases, the system begins relaxation to return to equilibrium (*Section 1.3.6*). While the system is out of equilibrium, the precessing magnetization in the transverse plane induces an electric current in the RF coil, which is the NMR signal. MRI also requires spatial information about the signals, which is only available through gradients (*Section 1.4.1*) [126].

1.4.1 Gradients

Spatial encoding is the process of signal localization from individual volume elements called voxels. Only the application of a third magnetic field (in addition to B_o and B_1) allows this process. This magnetic field is the gradient field that consists of three components (G_x, G_y and G_z). Individual gradient coils in the x-, y- and z-directions within the magnet bore are the gradient field source [126].

The slice select gradient (SSG) selects the slice of tissue for imaging. It is applied at the same time as an RF pulse so that only the protons that are within the selected slice are excited. The SSG is usually the first of three gradient pulses that is applied to the sample volume (as it was for experiments in this thesis). The phase encoding gradient

(PEG) determines the position of the spins in an orthogonal spatial dimension. The PEG shifts the phase of the signals along the direction of the PEG of the slice determined by SSG. Following SSG and PEG, the readout gradient or frequency-encoding gradient (FEG) can be applied. During this pulse, the signal is recorded and the frequencies of the signal encode the spatial information in the third spatial direction [126].

1.4.2 Spin echo sequence

A pulse sequence includes a sequence of RF and gradient pulses. Of the many different pulse sequences, the spin echo (SE) sequence is one of the most common [126]. It begins with a 90° RF pulse that uses an appropriate SSG. The 90° RF pulse flips the magnetization by 90° from the z-direction into the transverse plane. While the system is out of equilibrium, the magnetic moments dephase. After a period of delay by half the echo time (TE/2), a slice selective 180° RF pulse inverts M_{xy} to $-M_{xy}$. As a result, the magnetic moments rephase at a time of TE producing an increase in signal (called a SE). The SE is independent of any effects of field inhomogeneities. The magnitude of the signal depends on the T2 of the sample and the chosen TE of the sequence. Before the time TE, the PEG is applied, and at the time TE, FEG is applied. The application of additional 180° pulses spaced out in time by TE leads to more SEs obtained half way between the 180° pulses. The amplitudes of the collected SEs decay exponentially with the time at which they are collected after the 90° pulse [124]. To collect an entire image, the entire sequence of pulses is repeated many times. The time between 90° pulses is known as the repetition time (TR). The MR signal also depends on the T1 of the tissue being studied and the chosen TR.

1.4.3 Constructing a MR image

Signal processing in MRI digitizes (i.e., converts an analogue signal into digital form) a time-dependent signal for computer recognition. The digitized MR signals can be stored as k-space based on phase and frequency encoding. After multiple gradient and RF pulses, a two-dimensional map of k-space can be produced. For the SE sequence (*Section 1.4.2*), following every 180° pulse, one line of k-space is collected. A two-dimensional Fourier transform of the frequency domain data (of k-space) into the position-space data (i.e., the image) is required for data acquisition. The third dimension of an image is determined by the chosen slice thickness, and is obtained using slice selection (*Section 1.4.1*) [126].

1.4.4 MR image composition

The resultant MR image comprises of many picture elements (pixels) or voxels that hold numerical value. This value is directly proportional to the amount of signal obtained from the pixel or voxel. The size of the voxel is given by the spatial resolution that is determined by the matrix, field of view (FOV) and slice thickness [124]:

$$\text{Voxel Size} = [FOV_x/Matrix_x] \times [FOV_y/Matrix_y] \times \text{Slice Thickness}$$

MRI frequently employs square matrix sizes that are a power of two (e.g. 64, 128 or 256) pixels in each of the in-plane directions (recall FEG and PEG). FOV presets the area (in mm^2 or cm^2) from where the MR signals are collected. The matrix size, FOV and slice thickness can be customized to achieve high-resolution images.

Consequences in setting parameters (e.g., FOV, matrix size and slice thickness) to minimize image voxels for high-resolution images are decreased signal and/or increased

scan time. Lengthened scan time enhances the likelihood for animal movement, which then produces blurry images and most often renders the images useless. The intensity of the signal in each pixel depends on the type of sequence that is used.

1.4.5 T2-weighted MRI

At high fields such as B_o = 7.0 T, T2-weighted (T2W) MRI is required for image contrast as opposed to T1-weighted (T1W) MRI which is used for clinical field strengths. At increased B_o, T1 relaxation times are much closer to each other and provide little to no grey-white contrast [128]. T2 differences are greater and therefore provide more contrast. T2W MRI makes the signal intensity of a pixel dependent on the T2 value of the tissue within the pixel. This is achieved by reducing T1 dependencies by extending TR (e.g., more than 2,000 ms for the brain at B_o = 7.0 T) and by accentuating T2 decay by lengthening TE (e.g., 15-75 ms for the brain at B_o = 7.0 T) [127]. Tissues with longer T2 maintain M_{xy} longer and therefore appear brighter in a T2W image. In the brain, CSF with long T2 is bright, grey matter with intermediate T2 is intermediate and WM with short T2 is dark [126].

1.4.6 T2W MRI applications for EAE

Compared to computed tomography (an alternate imaging modality), T2W MRI of MS brain pathology is more sensitive to lesions [129]. T2W MRI is also useful in studying animal models such as EAE. The hallmarks of MS, as seen with conventional MRI, include enhanced T2 signals that produce hyper-intensities where lesions are

present. These lesions might correspond to a multitude of pathological changes such as inflammation, edema, demyelination, axonal loss and gliosis [130-133]. The signal increase reflects mobility of water protons and their reduced restriction that can occur in both MS and EAE. Just as T2W hyper-intensities are present in early MS lesions, they can be present in EAE and correlate positively with inflammation and losses of both myelin and axon integrity [134].

Although T2W MRI is a sensitive method to detect disease processes, it cannot specify MS lesions [135,136]. Additionally, the changes in T2W hyper-intensities are not always consistent because the degree of signal loss or gain varies. Variations in hyper-intensities reflect lesion activity (i.e., diminishing or enlargement of lesions). A further disadvantage of T2W MRI is the poor correlation between T2W lesions and patient disability [135,137,138]. Similar lesion heterogeneity in EAE models also occur [128]. Thus, the current status of T2W MRI is of limited use because the technique is not absolute in specifying pathological changes.

1.4.7 Diffusion-weighted imaging

Diffusion-weighted imaging (DWI) is a method that quantifies water molecule diffusion in three dimensions and might overcome the lack of (T2W) lesion specificity. As an advanced imaging technique, DWI can determine some physical features of a tissue (i.e., orientation, size and geometry) [139,140]. DWI studies can detect pathological changes in regions that correspond with T2W lesions and also in regions of normal appearing brain tissue as visualized by conventional MRI [139,141]. In fact,

various MS studies [139,142-145] show WM disruptions with DWI that are not apparent with T2W MRI.

Diffusion is the process in which molecules move from one location to another. At thermal equilibrium, the resultant diffusion of water molecules is from the Brownian (random) motion of water molecules. The intrinsic self-diffusivity or free diffusion coefficient (D) of molecules is described by Einstein's equation in one dimension:

$$r^2 = 2\,D\,t$$

The r^2 represents the mean squared displacement and t is the time of diffusion [146].

The diffusion of molecules within a biological system encounter physical constraints because of inherent biological structures (e.g., macromolecules, organelles, cell membrane, axon-membranes etc.) [147]. Highly organized tissues such as WM restrict molecular mobility and decrease the measure of diffusivity. This diffusivity is distinct from the intrinsic D. The term apparent diffusion coefficient (ADC) is the diffusivity that reflects the restriction of motion imposed by biological structures and is less than D [148,149]. In fact, biological barriers could reduce the diffusion by a factor of two to five (i.e., ADC of tissue water is less than D of bulk water) [150,151]. More accurately, ADC represents a bulk-mean estimate of diffusivity from many spins contained within a voxel [152].

The diffusivity of water molecules (whether D or ADC) is measurable with DWI using a pulsed gradient SE sequence by the Stejskal-Tanner equation [153]:

$$I = I_o\, e^{-TE/T2}\, e^{-b\,ADC}$$

The observed signal intensity is I. I_o is the signal that would be observed with a SE sequence that has no applied diffusion gradients. Recall that TE, T2, and ADC are echo

time, T2 relaxation time, and apparent diffusion coefficient, respectively. The b (or 'b-value') is a single scalar quantity (with units of time/distance^2) that represents the diffusion weighting and is specific to the pulse sequence being used.

In this thesis, four DWIs per direction are collected, each one using a different b-value. Data from these images are fit to the Stejskal-Tanner equation to calculate ADCs. In a plot of the natural log of I/I_o against b, the negative slope of the resulting line is the ADC. The direction of the diffusion gradients used in the imaging sequence gives the direction of the resultant one-dimensional ADC map. That is, the b in x-, y- and z-directions provide the basis for the ADC_x, ADC_y and ADC_z maps, respectively. The mean ADC (ADC_{mean}) is the mean of ADC_x, ADC_y and ADC_z.

DWI might be a useful tool for MS and EAE studies because disrupted WM might modify water molecule diffusion and ultimately change the ADCs. In fact, several animal investigations report changes with diffusion imaging during the course of WM disease. These include changes in diffusivities and anisotropy [112,154-160].

1.4.8 DWI applications for EAE

If the ADC in a biological system differed in three dimensions there would have been anisotropy in the measured diffusion. Anisotropy was first reported by Moseley and colleagues [161] who applied the Stejskal-Tanner SE sequence [153]. Moseley and colleagues found that the ADC longitudinal to the axonal tract ($ADC_{\parallel}$) was greater than in the perpendicular ($ADC_{\perp}$) direction. The myelinated axons might have hindered the molecular movement of water across the axon walls.

Common anisotropic calculations include relative anisotropy (RA) and fractional anisotropy (FA). However, the simple ratio between the different directional ADCs (i.e., $ADC_{\parallel}/ADC_{\perp}$) can represent the magnitude of anisotropy [162]. The standard deviation of the components of the more sophisticated diffusion tensor imaging (DTI) method is used to calculate the RA and FA.

In this thesis RA and FA were not calculated because DTI could not be performed. Instead DWI was performed, which required the approximation of $ADC_{\perp}$ and $ADC_{\parallel}$ values by the directional ADC values (*Section 2.4.3*):

$$ADC_{\perp} \approx (ADC_x + ADC_y) / 2$$

$$ADC_{\parallel} \approx ADC_z$$

Irrespective of the EAE model, the putative DWI markers under evaluation are $ADC_{\perp}$ and $ADC_{\parallel}$. In WM, increases in $ADC_{\perp}$ values suggest myelin damage [154-158]. Some animal models with axonal damage report decreases in $ADC_{\parallel}$ [156,159]. Changes in ADC_{mean} and diffusion anisotropy are less specific to WM disease pathology [159,163,164]. Inflammation and/or edema cause increases in ADC_{mean} [165]. The overall change in $ADC_{\perp}$ and/or $ADC_{\parallel}$ due to any/all of these WM disease pathology reduces anisotropy [166,167]. These patterns describe more than one disease process. The skepticism in establishing robust correlations between DWI metrics and lesion activity limits this imaging technique to research [162,168-170]. Nonetheless, DWI metrics (i.e., ADCs and anisotropy) might provide invaluable clinical applications such as increased sensitivity for lesions compared to T2W MRI [139,141]. This suggests that DWI might potentially provide a better imaging tool to evaluate MS.

1.4.9 Small animal imaging

Imaging small animals usually operates at ultra high B_o compared to clinical MRI (i.e., 4.7 to 17.6 T versus 0.4 to 3.0 T) [128,171]. The greater B_o allows for the necessary resolution to delineate disease (e.g., EAE) pathology [172]. While increased B_o is a step in the right direction to improve the overall image quality, there are always costs.

At higher field strengths, contrast-to-noise ratios differ. T1 and T2 are less distinct and provide less contrast in a particular weighted image. For example, T1W MRI at high fields provides little contrast between tissues [128]. Other consequences originate from maximizing image quality, which depend on the signal to noise ratio (SNR), acquisition time and spatial resolution. Optimizing spatial resolution (and good SNR) is the paradoxical goal in small animal MRI because the tradeoff typically is longer acquisition time.

The theoretical spatial resolution, considering the Brownian motion and the typical times for imaging (10-100 ms), is 10 μm [173]. Experimentally, the poor SNR (that originates from the initial selection of small voxels) makes this resolution virtually unachievable. The increase in B_o and in the number of excitations (NEX) improves the SNR but also increases the odds of artifacts and acquisition times. Physiological (e.g., blood flow and respiration) and physical (e.g., head shifting) motions, in addition to the molecular diffusion of water, contribute to movement in *in vivo* animal studies. After considering all the determinants affecting small animal MRI, the typical *in vivo* resolution is closer to 10 times the theoretical range (i.e., 100 μm) [173]. With the advent of stronger MR scanners and better pulse sequence development, the resolution is becoming closer to the theoretical limit.

Despite the difficulties at high B_o, a well-planned pulse sequence can maximize image contrast for animal studies. One example is the Stejskal-Tanner SE sequence that can specify imaging parameters such as TR, TE and b for a specifically weighted (e.g., T1W, T2W, proton density-weighted and diffusion-weighted) image. Pathological changes also affect these parameters and provide further contrast differences with progressive disease. Longitudinal T2W and DWI studies of EAE lesions are applications of small animal imaging with sufficient contrast-to-noise ratio.

The mice in this thesis were imaged at B_o = 7.0 T. Due to the complexities involved with this (ultra high) magnetic field strength, a clinical sequence was not applied nor was it appropriate [128]. Instead, a modified laboratory sequence was used.

1.5 Aims of the study

EAE, an animal model of MS was utilized to investigate the pathological effects of disease on the optic chiasm. Specifically, monophasic EAE was selected because of interest in studying EAE lesions in the optic chiasm with DWI. DWI was performed to calculate the ADC in the x-, y- and z-directions for possible lesion specificity. That is, DWI experiments were performed in order to test the following putative markers in the optic chiasm of EAE mice:

A) Increase in $ADC_{\perp}$ (i.e., $ADC_{\perp} \approx (ADC_x + ADC_y) / 2$) to reflect myelin damage,

B) Decrease in $ADC_{\parallel}$ (i.e., $ADC_{\parallel} \approx ADC_z$) to reflect axonal damage,

C) Increase in ADC_{mean} to reflect inflammation and/or edema, and

D) Significant change in anisotropy (i.e., approximated by a decrease in $ADC_{\parallel} / ADC_{\perp}$) as a result of EAE.

In order to test the above hypotheses, this thesis included:

- EAE induction with MOG_{35-55} and adjuvants to study lesions in the optic chiasm of mice.
- T2W MRI and DWI of the mouse brain.
- Histological confirmation of lesions in the optic chiasm.
- Calculation of ADC values in each direction based on DWI.

CHAPTER 2: Materials and Methods

2.1 MOG_{35-55}-immunized EAE

The following investigations included seven separate experiments of 48 C57BL/6 female mice (*Appendix A*). The study groups included MOG_{35-55}-immunized mice (N=39), wild type control mice (N=6) and sham control mice (N=3) (Table 1). Mice were supplied from either Charles River Canada (St. Constant, Canada) or the Genetic Models Centre (Winnipeg, Canada) at 10 weeks old. For one week prior to the study, mice were acclimated (i.e., removed from their cage once daily one at a time to undergo basic holding and handling procedures).

Table 1. Summary of experimental mice.

Number of mice	Study group (inoculation)
6	Wild type control mice (no MOG_{35-55} and no PTX)
3	Sham control mice (PTX only)
39	MOG_{35-55}-immunized mice (MOG_{35-55} and PTX)

Female C57BL/6 mice (N=48) were classified into study groups: wild type control, sham control or MOG_{35-55}-immunized mice. Mice received both MOG_{35-55} and PTX inoculation for EAE induction. Sham controls received PTX only and wild type controls received no inoculations.

EAE induction began on day 0 (at 11 weeks of age) under isoflurane (1.5 to 2%) anaesthesia. Each mouse set out for EAE received two 50 μL subcutaneous flank injections of 0.5 mg/mL of rodent MOG_{35-55} (synthesized by the Peptide Facility of the University of Calgary) [174]. MOG_{35-55}, as previously described [175,176], was prepared in phosphate buffered saline (PBS) and further diluted 1:1 with CFA (Sigma Aldrich, St. Louis, MO, USA). MOG_{35-55} immunization was also accompanied by a 200 μL intraperitoneal injection of 0.3 μg of PTX (List Biological Laboratories, Campbell, CA, USA) in PBS. On day 2, EAE mice (N=39) received a second dose of PTX as described for day 0. (For a complete description on EAE induction, refer to *Appendix B*).

Of the remaining nine mice, designated wild type controls received neither MOG_{35-55} peptide, CFA nor PTX (N=6) while sham controls received solely PTX (N=3) as described above. The wild type controls sufficed as standard controls [112,119,160,177]. Sham controls were investigated because of the results of previous studies that included control mice that received the same EAE preparations without MOG_{35-55}. While there were no differences on the blood-spinal chord barrier [174], there were decreased amplitudes in VEPs [178]. Sham controls were studied as an alternative control to observe any effect of PTX on the optic chiasm.

Mice were housed in separate cages, fed *ad libitum* on standard chow and monitored for up to 29 days after immunization. Experiments were conducted under the guidelines of the Canadian Council on Animal Care and approved by The Institutional Animal Care Committee (ACC) at the University of Manitoba (protocol number 08-040).

2.2 Clinical scoring

Each mouse was assessed daily (commencing on day 3) by monitoring their bodyweight and motor functions. The EAE scoring system used was modified from a 0 to 5 scoring system as previously described [174,179]. (Refer to *Appendix C* for an example of the monitoring record sheet that was used for scoring).

Clinical scoring evaluated the tail and each limb separately from scores 0 to 2 and 0 to 3, respectively. In total, scores ranged from 0-14 and a score of 15 was reserved for any animal that died due to EAE severity. A score of 0 for each limb was given when there was no apparent loss of function. Limb performance was assessed by observing animal gait and evaluating limb grip. Each affected limb was given a score of 1 when the animal failed to hold on tightly upon suspension and began to fall. An unusual gait indicated which limb was affected. When signs of limb dragging and partial paralysis were present, the affected limb was given a score of 2. A score of 3 was assigned for any limbs that indicated full paralysis.

Tail function was tested by their ability to wrap around the examiner's finger. While 0 indicated no abnormality, a score of 1 was assigned when the tail seemed flaccid and a score of 2 was assigned when the tail was completely paralyzed. The old standard scoring system (i.e., scores that ranged from 0-5) was also included as part of the daily assessment as shown in *Appendix C*. When the mouse reached a standard score of 1, softened moist food (bacon softies) was provided in the cage. When a standard score of 2 was observed, 1 cc of saline was administered subcutaneously. Given the pilot nature of this study, the assessor was not blinded to the study groups.

2.3 MRI

MRI included T2W and DWI MRI protocols of mouse brains including the entire optic chiasm. Images were obtained using a Bruker Biospec spectrometer with a 7.0 T/21 cm magnet using a 20 mm internal diameter quadrature volume coil. The animals were positioned in the Bruker Biospec spectrometer so that the axonal tracts ran along the z-direction as best possible. For imaging purposes, mice were anaesthetized by ventilation with 1.5 to 2% isoflurane in O_2/N_2O via nose cone administration. During scan times (typically 92 minutes), animal respiration rates and external body temperatures were monitored. Temperature was maintained as best possible (36.5-38°C) by adding cool or warm air when needed and maintained as close to core values. An example NMR monitoring form and the NMR protocol for DWI are provided in *Appendix D and E*, respectively.

EAE mice were imaged at pre-disease (N=39) and at targeted onset (N=22) and peak (N=18) disease time points. Occasionally, imaging on the correct onset and peak time points were not always possible. This was because animal care protocols did not allow an animal to be anaesthetized on successive days, or too many animals needed to be imaged in a given day. Also, scheduling the Bruker Biospec spectrometer to predict disease outcome was problematic in targeting onset and peak EAE. The 'peak' imaging time had to be estimated because the score of an animal was not predictable. Sham (N=3) and wild type (N=6) controls were imaged at similar times points as EAE mice (i.e., the same mouse was imaged multiple times). Images that required better imaging results (because of image distortions) were repeated.

2.3.1 T2W MRI

T2W MRI was performed on mouse brains to include the optic chiasm within the FOV (2.5 x 2.5 cm^2). Other imaging parameters were: TR = 2,500 ms, TE = 27 ms and matrix size 256 x 256. Data from one 0.75 mm thick slice were collected with two averages. This resulted in a spatial resolution (i.e., voxel size) of 98 x 98 x 750 μm^3. The scan time for T2W MRI was 47 minutes.

2.3.2 DWI-derived ADC maps

ADC maps derived from DWI were obtained in the y-, x-, and z-directions, with four b-values = 189.1473, 336.2619, 525.4093 and 756.5894 s/mm^2 (*Section 1.4.7*). These b-values (randomly selected from the standard eight possibilities previously used in the lab) were applied in a consistent random order. This method was chosen to reduce the effect of drift on (the fit to the data for) ADC calculations. A modified TurboFLASH sequence [180] was applied with matrix size 128 x 128. Because of the inherently lower SNR in diffusion-weighted images when compared to T2W images, the slice thickness, FOV and NEX were increased to 1.00 mm, 4.0 x 4.0 cm^2 and 32, respectively. The resulting spatial resolution (i.e. voxel size) for each ADC map was 313 x 313 x 1,000 μm^3. Given the limitations of the Bruker Biospec spectrometer (*Section 4.5*), each gradient direction included a complementary scan per b-value. Therefore, the scan time for each direction was 15 minutes.

2.4 MRI analysis

All of the raw data obtained from the Bruker Biospec spectrometer were imported to a PC machine and analyzed with custom-written MATLAB scripts. The initial script loaded both the T2W and DWI images of all the brains that were imaged. Based on stereotaxic coordinates [181], the presence of the full optic chiasm was confirmed within the anatomical T2W images. The DWI images were also considered to also contain the optic chiasm because the slice of the DWI images (i.e., 1.00 mm) included the slice of the T2W images (i.e., 0.75 mm). All of the images were monitored for EAE hyper-intensities. However, ADC analysis in a pixel-by-pixel manner was only applied on animals that had successful pre-disease (N=12), targeted onset (N=11) and peak (N=11) disease images. A similar ADC analysis was performed on images obtained from wild type (N=11) and sham control mice (N=4). Therefore, the following procedures for MRI analysis were based on 49 sets of raw data.

2.4.1 Image registration

In the ADC analysis, customized scripts for MATLAB 7.1 produce four ADC maps (Figure 1) from DWI raw data (i.e., from all the b-values and complement). This allows pixel-by-pixel ADC value analysis for any region of interest (ROI) or point of interest (POI) within the resultant image. While the ROI includes numerous pixels within a region, the POI refers to the selection of a single pixel.

If there is any motion during DWI, image artifacts can occur. These image artifacts would produce unreliable ADC calculations because each pixel-by-pixel ADC

calculation depends on every diffusion-weighted image. Therefore, any image acquisition following unwanted brain re-positioning requires image registration to re-align the pixels.

Figure 1. DWI-derived ADC maps.

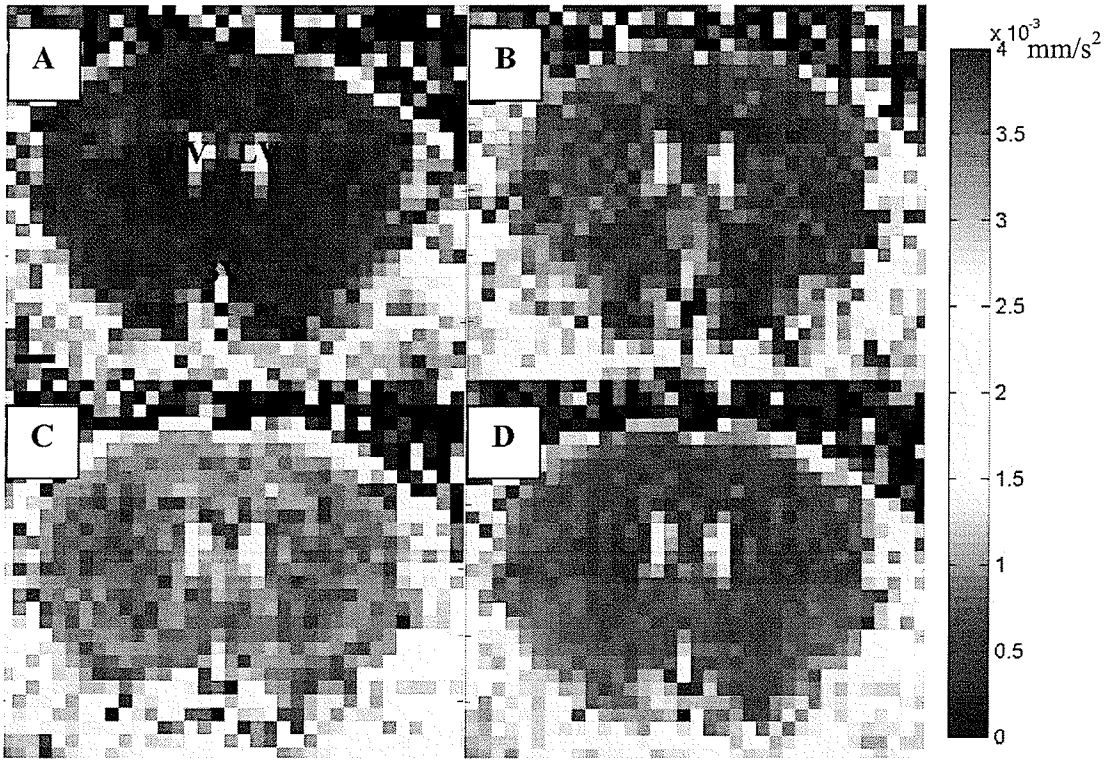

One example of four ADC maps obtained from a wild type control mouse. ADC_x (A), ADC_y (B), ADC_z (C) ADC_{mean} (D) maps were calculated with a customized MATLAB 7.1 program using DWI raw data. Normal anatomical regions of hyper-intensities included the lateral ventricles (LV) and third ventricle (3V) (A) indicative of the inherent diffusion of water (i.e., faster in the ventricles). The remainder of the brain was more homogeneous in intensity. ADC values measured from each pixel [mm^2/s] were quantified based on a colour scale (right). Bar = 3 pixels = 939 μm (A).

Banding artifacts around the surface of the brain in ADC maps were a good indication of the occurrence of movement between scans. Under these conditions, image registration (N=3) was first applied to DWI images prior to ADC calculation (*Section 2.4.2*). All other diffusion-weighted images (i.e., without motion artifacts) proceeded directly to ADC calculation (N=46). Recall that DWI consisted of eight images per direction (i.e. a complementary image per b-value given the hardware limitations and four b-value images per direction). For the data sets requiring registration, these images were viewed through an image registration MATLAB program that allowed manual re-positioning of the images. The goal of image registration was to shift or register images so that the brain was placed back in the position it was prior to movement. Possible shifting could have occurred at any of the following time points:

A) Between a b-value image and its complementary image,

B) Between one b-value image and the next b-value image, and

C) Between one directional image (i.e., the last b-value for the direction) and the next directional (first b-value) image (e.g., between y-direction and x-direction).

The manual registration MATLAB program loaded raw DWI data and images were viewed in the order in which they were acquired.

Any necessary registrations were performed in an order that first addressed case A then B then C. That is, the b-value image (not its complement) of the first b-value applied in the y-direction was first viewed and compared to the complementary image of the same b-value in the same y-direction. If the brains appeared misaligned between a pair of consecutive images, manual registration was applied. This involved appropriate

translations in the x- and/or y-directions and rotations in the angle of the brain. All changes were made in the order relative to the first image collected.

Any shifts in case A would have been somewhat less complicated to detect. However, image registrations would have been more difficult because the consecutive changes were not automated. Shifts occurring in case B and C were more cumbersome to detect but fewer changes were required after the initial manual registration. In any case, shifted images were corrected by minimizing the artifacts in the calculated ADC_{mean} map as best possible. Changes were saved for post image registration ADC calculations. For all manually registered cases (N=3), translations were required between y-direction and x-direction images (i.e., case C). This made the detection the most cumbersome but fortunately required fewer changes.

2.4.2 ADC calculation

Due to the machinery limitations, each b-value (N=4) image was actually composed of two images (i.e. four b-value images and their respective complementary images per direction were required for DWI). A MATLAB script provided a means to examine the signal intensity in each pixel at each b-value. By plotting the natural log of the signal intensity against b-value, four points were fitted to a straight line for each pixel. This method produced a negative slope and the negative value of this slope was the ADC within the single pixel.

Artifacts due to eddy currents compromised the accuracy in ADC calculations. A single poor image in DWI would have offset the line of best fit (of four points) if one of the points were inappropriately out of range. In these conditions, an automated program

(Viewer Reg, MATLAB script) fitted a line to only three points and measured the distance between the line and the ignored point. This procedure was repeated four times, and ignored each b-value once. Rather than calculating ADC maps out of four b-values, ADC maps were produced by removing one outlier b-value and fitting to three. The point that was the furthest away from the line fit was taken to be the outlier b-value for the pixel. While the automated code detected the outlier b-value per pixel, variations in outliers were possible amongst pixels comprising a single image. Therefore, in addition to automated outlier calculations, manual examination was required. The calculated ADC value fitted to three points would have otherwise been based on (three) different b-values varying per pixel. This would have led to incorrect ADC calculations because only one b-value image (i.e., the image that was most out of range) omission was allowed.

Fortunately the automated program calculated the number of times each b-value was ignored (in deriving the directional ADC maps). The most ignored b-value was designated as the outlier and coincided well with the poor quality b-value image. For example, images with greater b-values had increased diffusion weighting, by definition, and thereby resulted in darker images. If this trend was not observed within a particular b-value image then the particular b-value was suspected as an outlier. In this thesis 13 DWI results were re-fitted with the removal of an outlier b-value (i.e., each only included three of the four b-values).

2.4.3 Selecting the ROI and POIs

The chosen ROI for these experiments was the lateral edges of the optic chiasm. If no pathological changes occurred within EAE mice, the optic chiasm could have been represented by three to five pixels. However, the selection of pixels for pixel-by-pixel ADC analysis was based on the following, which indicated that pathological changes were concentrated at the lateral surfaces of the optic chiasm:

- EAE histology showed inflammatory cells near and on the lateral chiasm surfaces. Edema and changes in chiasm, subarachnoid and perivascular space thickness (*Section 3.3*) were also observed.
- EAE ADC maps displayed a segmented row of hyper-intense pixels below the third ventricle (i.e., the ROI). Iso-intense (i.e., the same in intensity as the rest of the brain) pixels were commonly found in the medial regions typically segmenting the hyper-intense pixel regions by two to three pixels.
- In some cases, ADC values were just plain out of range. The noise outside of the tissue (i.e., the brain) was greater than the signal intensity and led to inconsistent ADC calculations such as negative values. Therefore, POIs that measured negative ADC values that were sometimes found in medial region were avoided.
- A partial volume effect resulted when different tissues shared space within a single pixel. This blurred pixel intensity and made the selection of ROI and/or POI difficult.

Therefore, rather than selecting consecutive three to five pixels for data analysis, six pixels divided equally (i.e., three on either side) by either two (N=35) or three (N=14) pixels were chosen (Figure 2). POI selections were not always symmetrical because of

the angle and/or orientation of the brain. Because hyper-intensities in ADC maps were also evident in the pixels below the primary segmented row described (row A), an additional segmented row (row B below row A) was also studied. Row B was considered to contain some of the optic chiasm for similar reasons listed above (i.e., due to the enlargement, partial volume effects and inflammation). The nomenclature for these POIs is shown in Figure 2.

Figure 2. Nomenclature for pixels making up ROI.

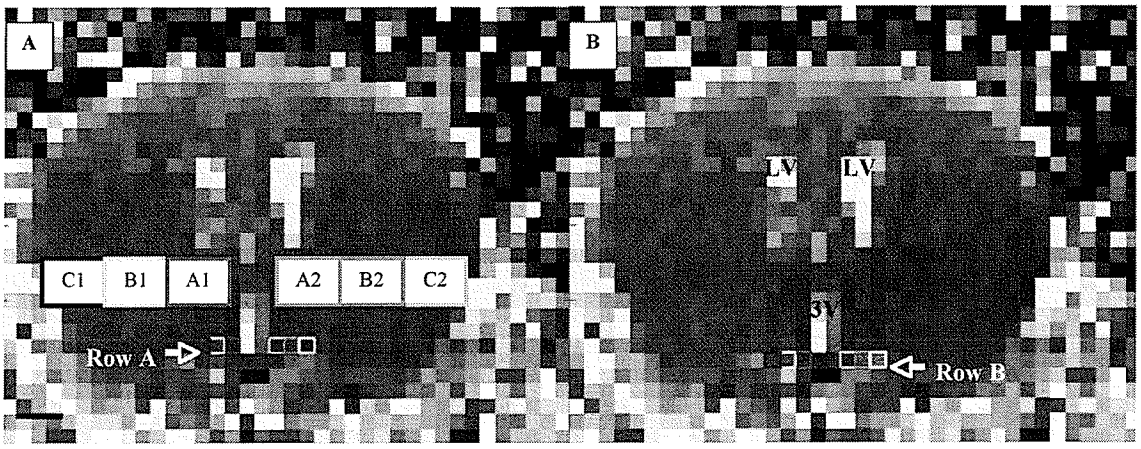

The nomenclature for the six pixels that made up the ROI: row A (A) and row B (B) from the same ADC_{mean} map. A single pixel represented a single point of interest (POI). Both rows included two separate groups of three POIs (i.e., C1 through A1, and A2 through C2) one on each side of the third ventricle (3V). In this example, the 3V was two pixels wide (i.e., two pixels segment both rows). The pixels that made up row B were directly below row A pixels. Normal anatomical regions of hyper-intensities included the lateral ventricles (LV) and 3V (B). Bar = 3 pixels = 939 μm (A).

Recall that the mouse was positioned in the magnet bore with the goal that the axonal tracts would run in the z-direction. The DWI-derived ADC maps provided ADC

values for the x-, y- and z-directions. These ADC_x, ADC_y and ADC_z values were calculated for each POIs and used to approximate the directional ADC values (i.e., $ADC_{\perp} \approx (ADC_x + ADC_y) / 2$ and $ADC_{\parallel} \approx ADC_z$).

2.5 Tissue processing

Animals were euthanized with cardiac perfusion of either formalin or glutaraldehyde at the end-of-study under isoflurane (1.5 to 2%) anaesthesia. Ten percent formalin (N=4) was used for perfusion when tissue was needed for basic histology. When the tissue was prepared for plastic section and electron microscopy (EM) 2% glutaraldehyde (N=38) was used for perfusion.

Tissue was collected from all mice that underwent cardiac perfusion, while no tissue was collected from mice euthanized by the ACC (N=6). The ideal end-of-study was peak disease. However, peak disease was only achieved in retrospect to the full clinical course of the disease per animal. As a result, euthanasia of EAE mice was performed at the estimated time for peak disease. The days in which the estimated peak disease was missed was calculated from the day the maximum score was obtained (Table 2). The state of each animal at the time of euthanasia is defined in Table 2.

Table 2. Defining the end-of-study at the time of euthanasia.

Number of mice	State of animal when euthanized
4	Peak disease
5	One day past peak
3	Two days past peak
1	Three days past peak
1	Four days past peak
1	Five days past peak
1	Eight days past peak
1	Ten days past peak
2	Eleven days past peak[1]
14	No signs of EAE ever presented[2]
6	Required humane euthanasia[3]
6	End for wild type controls
3	End for sham controls

The state of each animal at the time of euthanasia as defined. No tissues were collected from the following mice that were euthanized by the ACC: Mice were euthanized [1]eleven days post peak disease (N=2) because greater scores were anticipated, [2]after no signs of EAE by the end of the experiment (N=1) and because of [3]tail loss (N=2) and bald skin lesions (N=1).

Some MOG_{35-55}-immunized mice were euthanized for tissue processing without ever showing signs of EAE (i.e., all zero scores, N=13). Other mice were euthanized for

tissue processing because humane endpoints were reached (N=3). Given that a tissue collection protocol was not included in the first set of experiments, some mice were euthanized without tissue collection at:

A) Eleven days post peak disease (N=2) because greater scores were anticipated based on a previous study [174],

B) The end of the group study after having shown no (clinical) EAE (N=1), and

C) Various times when humane euthanasia was required (N=3).

Humane endpoints for EAE (N=6) included decrease in body weight (of 30% that persisted for more than two days), signs of urine scalding, and a standard score of four or signs of rapidly increasing disease. Some mice required humane euthanasia because of self-mutilation such as scratching and/or biting the tail or coat. These conditions led to tail loss (N=3, tissue collected from one mouse), bald skin lesions (N=1, no tissue collected) and abscess formation on the hind limb (N=1). Humane euthanasia was also required when there was a sign of rapidly increasing disease (N=1) (ACC, personal communication, 2007).

Following cardiac perfusion, brains were removed (N=42) and stored overnight in immersion fixation at 4°C in either 10% formalin or 2% glutaraldehyde. Because all the mice were treated the same (with respect to their study group), only a few of the fixed brains were selected for further tissue processing. Tissues from EAE mice (N=4 for basic histology, N=4 for plastic section microscopy and EM) were selected to represent the pathological changes. Comparable tissues were collected from sham controls (N=2 for plastic section microscopy and EM) and wild type controls (N=2 for plastic section microscopy and EM).

2.5.1 Basic histology

Fixed brains (N=2) of EAE mice were excised and divided into 4 mm sections that included the optic chiasm in order to fit plastic cassettes for histology. These brains were obtained immediately after mice were imaged two and four days after peak EAE. Tissues were then dehydrated and embedded in paraffin wax. Six 5 μm slices were taken every 250 μm and stained with standard Harris Hematoxylin and Eosin Y (HE) and Solochrome Cyanin (SC). HE and SC slides were examined for general features of inflammation and demyelination, respectively (Olympus BX51 Research Microscope – Bright-field). Images were taken at 12.5x, 40x and 200x magnifications (Leica FireCam software). Because it was immediately apparent that light microscopy on paraffin-embedded samples would not offer the information needed to interpret the MR changes, subsequent tissues were processed for plastic embedding.

2.5.2 Plastic section and electron microscopy

Optic chiasma of EAE (N=4) and control mice (N=4 i.e. 2 sham controls and 2 wild type controls) were extracted from previously removed and fixed brains (*Section 2.5*). The end-of-study for these EAE mice was defined as one day after peak EAE score. Control mice were euthanized to match this end-of-study time. The optic chiasma were approximately 0.24 mm in thickness. With the aid of a stereoscopic dissecting microscope and visualization of the optic tracts, left and right sides of the chiasma were marked. Tissues were stored in 2.5% glutaraldehyde and PBS for transfer, and for plastic

section microscopy and EM preparations. The preparations for plastic section microscopy and EM as directed by the Department of Pathology at the Health Science Centre were included in *Appendix F*. Dr. Marc Del Bigio, blinded to the study groups, examined both semi-thin (0.5 μm) and thin sections (80 nm) for myelin and axonal damage (JEOL 1010 – transmission electron microscope).

2.6 Statistical analysis

Forty-nine (*Section 2.4*) DWI data sets underwent pixel-by-pixel ADC value (i.e., ADC_{mean}, ADC_z and approximated $ADC_\perp$) analysis of rows A and B. POI (i.e., A1 through C2 comprising of rows A and B) ADC values obtained from images of sham (N=4), wild type (N=11) and pre-disease (N=12) controls were compared by one-way analysis of variance (ANOVA). POI ADC values measured from pre-disease (N=11), onset (N=11) and end-of-study (N=11) DWI results were analyzed by repeated measures ANOVA followed by Duncan's tests. While the included pre-disease images were obtained within nine days of immunization, the targeted onset and peak (i.e., ideal end-of-study) images included in the analysis were obtained at targeted time points no later than three days (Table 3). From herein, references to targeted onset and peak will be referred as just 'onset' and 'peak' (e.g., MRI at onset and peak). Statistical tests were considered significant at a level of $p<0.05$. These statistics were performed at the National Research Council (Institute for Biodiagnostics, NRC, 435 Ellice Avenue, Winnipeg, MB) by application of the STATISTICA software (StatSoft, Inc., 2300 East 14th Street, Tulsa, OK 74104 USA) and directed by Mr. Randy Summers, the onsite statistics services officer.

Further one-way ANOVAs were performed to evaluate the mean anisotropies (i.e., approximated by ADC_z / $ADC_\perp$) with respect to EAE progression. The Student T-test was used to compare the mean (of all POI) $ADC_\perp$ and ADC_z values. Statistical tests were applied for values measured from both rows A and B, and were considered significant at a level of $p<0.05$. These tests were performed on SPSS Statistics 17.0 (SPSS Inc. Headquarters, 233 S. Wacker Drive, 11th floor, Chicago, IL 60606 USA).

Table 3. State of EAE of the images used for analysis

A.

Number of mice	Day of pre-disease image (Day 0 being day of immunization)
4	Day 0
4	Day 1
1	Day 2
1	Day 3
1	Day 5*
1	Day 9

B.

Number of mice	State of EAE at targeted onset image
8	Onset disease
3	One day past onset

C.

Number of mice	State of EAE at targeted peak image[†]
5	Peak disease
4	One day past peak
1	Two days past peak
1	Three days past peak

State of EAE at pre-disease (A) and at targeted onset (B) and peak (C) imaging of the images used for analysis (N=49). [*]The image of this animal was only included for one-way ANOVA (*Section 2.6*). [†]The day in which the animal imaged for peak disease was in retrospect to their EAE progression.

CHAPTER 3: Results

3.1 MOG_{35-55}-immunized mild monophasic EAE

The outcomes of all the MOG_{35-55}-immunized mice (N=39) are summarized in Table 4. While 23 mice exhibited signs of EAE before euthanasia, some showed no signs of EAE (N=14). Others developed non-EAE conditions that required humane euthanasia (N=2) (*Section 2.5*). More specifically, 59% of MOG_{35-55}-immunized mice showed signs of EAE while 36% did not and 5% developed non-EAE conditions that required humane euthanasia. Although not shown in Table 4, no clinical signs of EAE were observed in sham (N=3) and wild type (N=6) control mice.

Table 4. Summarized outcomes of MOG_{35-55}-immunized mice.

Number of mice	Outcome of MOG_{35-55} immunization
23	Signs of EAE present before euthanasia
14	No signs of EAE present before euthanasia
2	Developed non-EAE conditions requiring humane euthanasia*

The outcomes of MOG_{35-55}-immunized mice (N=39) prior to euthanasia were: signs of EAE, no signs of EAE and the development of non-EAE conditions that required humane euthanasia. *These conditions (self-mutilation that led to tail loss and hind limb injury) were suggestive of pain and distress (*Section 2.5*) and were recommended for humane euthanasia by the ACC at the University of Manitoba.

Figure 3 shows the mean outcome of EAE in C57BL/6 mice (N=23). A correlation between the onset of EAE and the decrease in body weight was apparent. Prior to EAE onset the body weight showed an increasing trend. EAE onset (i.e., increased clinical score) typically occurred with weight loss. Some EAE mice (i.e., 16 of 23) experienced weight loss 1-5 days (mean=1.9 days) prior to EAE onset. Other weight losses (i.e., 7 of 23 mice) occurred concurrently with disease. While many studies simply correlated typical weight loss with EAE onset [182], some studies reserved weight loss as a preclinical symptom [183].

Figure 3. Signs of EAE progression.

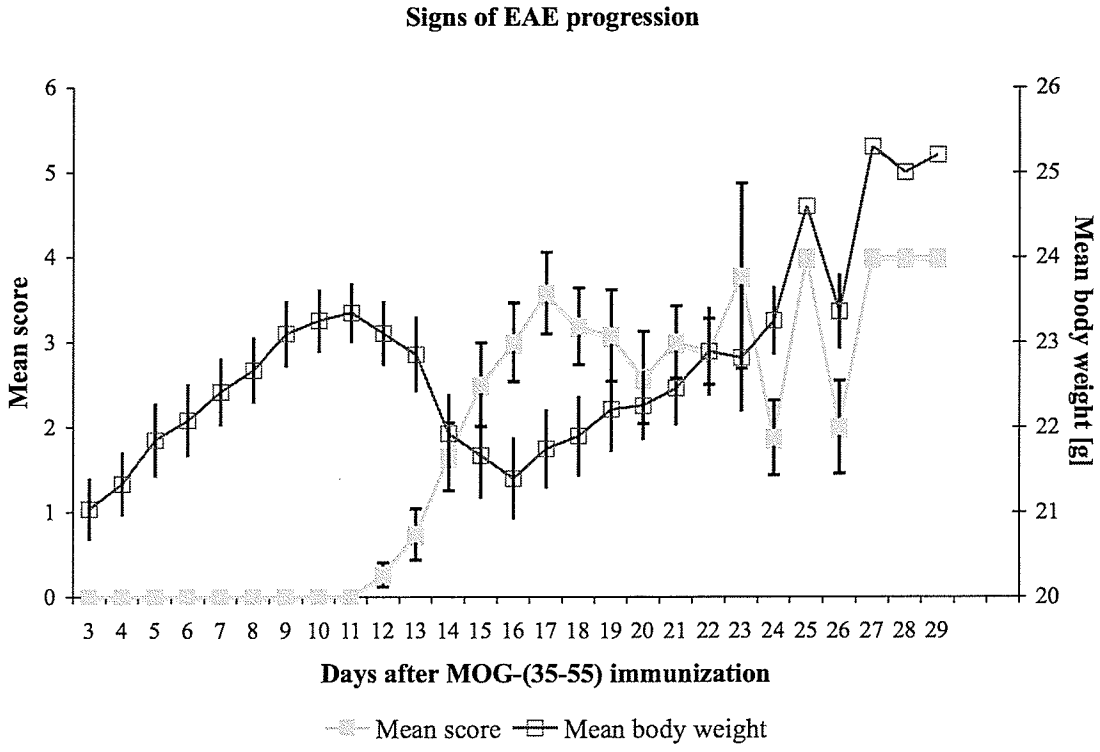

Increases in the mean scores (—■—) paralleled the loss in mean body weight (—□—) in mice (N=23) following MOG_{35-55} immunization. Mean scores were based on a 0 to 14 scoring system. Error bars represent the standard error of the mean (SEM).

EAE onset ranged between 12-20 days following inoculation. The first sign of EAE was normally detected by weight loss and/or tail disability. The time to peak disease (i.e., when the animals reached its maximum score) ranged from day 13 to day 23. Typically, by this time in the disease, tail function was completely lost (i.e., tail score=2, N=22) while hind limbs experienced variable motor disability.

3.2 MRI

Both T2W and DWI MRI techniques were applied amongst 48 animals resulting in 95 coronal image sets of the brain throughout EAE development. Image sets included one 0.75 mm slice with eight SEs for T2W MRI (Figures 4A-H) and one 1.00 mm slice for DWI. DWI was performed in each direction (which each required four b-value applications and a complementary scan per b-value). In other words, each diffusion-weighted ADC map (i.e., ADC_x, ADC_y, and ADC_z) was calculated from four b-value images plus their respective complementary scan (Figures 4I-L). ADC_{mean} was calculated as the mean of ADC_x, ADC_y and ADC_z. Figure 4 is one example of an image set obtained from one EAE mouse imaged at pre-disease.

Figure 4. MRI of a single mouse brain at pre-disease.

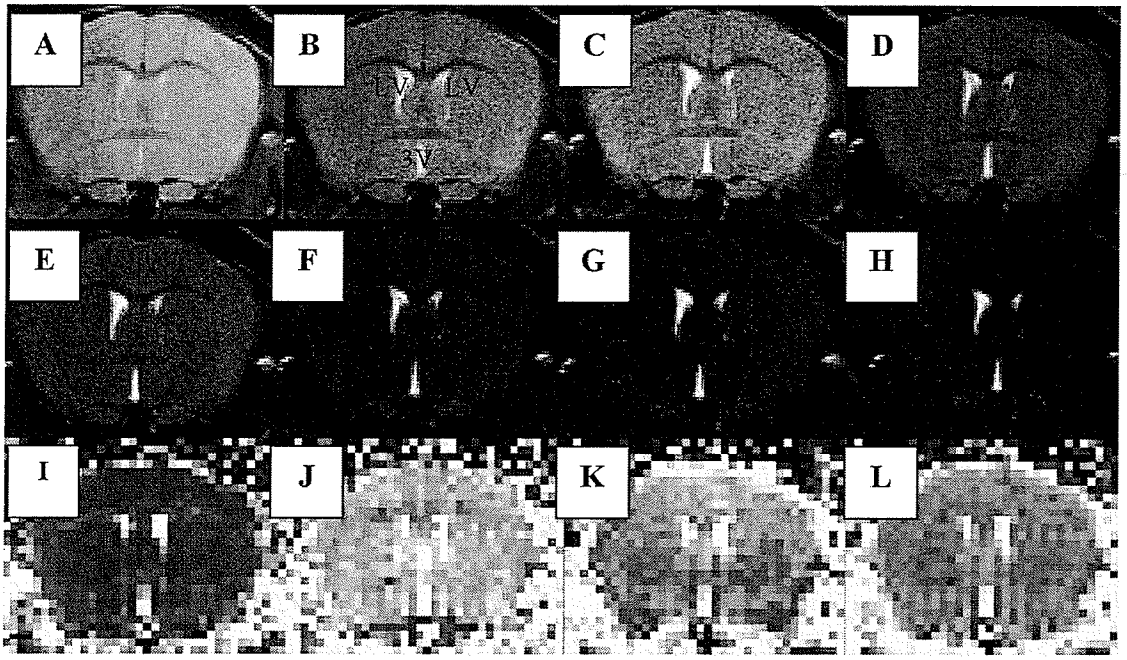

A single MR image set included eight SEs from T2W MRI (A-H) and DWI-derived ADC_x (I), ADC_y (J), ADC_z (K) and ADC_{mean} (L) maps. Normal anatomical regions of hyper-intensities for both MRI techniques included the lateral ventricles (LVs) and third ventricle (3V) (B). ADC values (I-L) were colour scaled as shown in Figure 1. Bar = 3 pixels = 939 μm (I).

3.2.1 T2W lesions with EAE

All coronal sections of T2W MRI included normal anatomical regions of hyper-intensities: lateral and third ventricles (Figure 5). Small regions of hyper-intensities (localized in the region of the trigeminal nerves) were observed in some T2W MRI of sham (N=3), wild type (N=2) and pre-disease (N=9, not shown) mice. These regions did not include the optic chiasm nor did they appear to worsen with EAE. Thus study of

these areas was left for future experiments. T2W MRI at EAE onset (Figure 5B) and peak (Figure 5C) showed hyper-intense signals (T2W lesions) in the region of the optic chiasm with EAE disease. While enlarged ventricles were also observed with disease, severity was inconsistent. Analogous to pre-disease T2W MRI, no T2W lesions of EAE insults were observed in wild type (Figure 5D) and sham controls (Figure 5E).

Figure 5. One SE of a T2W image obtained from C57BL/6 mice.

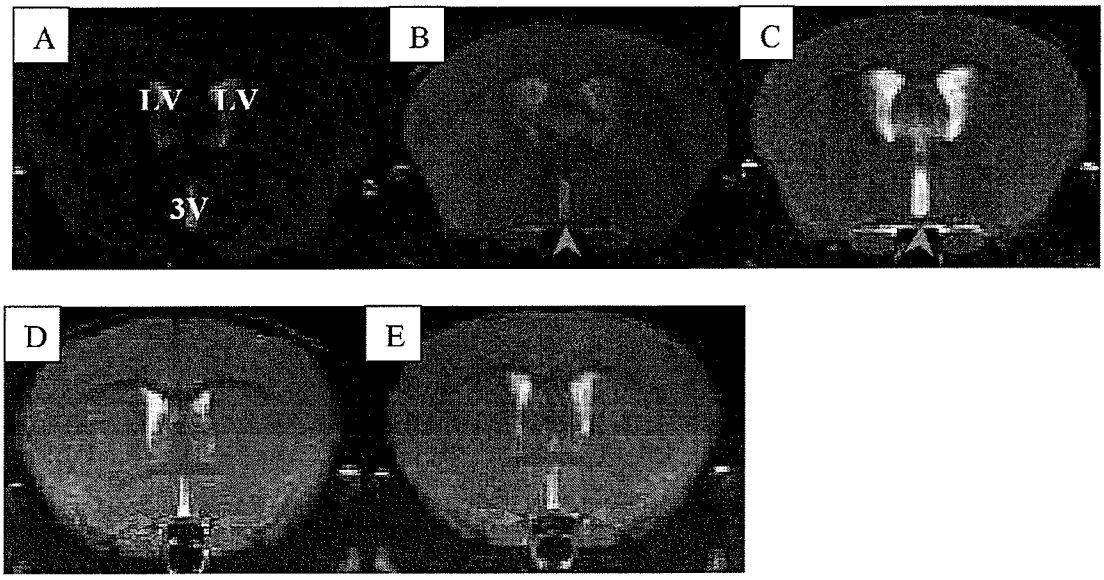

Coronal sections of the experimental mice included the lateral ventricles (LV) and the third ventricle (3V) as normal anatomical regions of T2W hyper-intensities (A). T2W lesions (arrow heads) were present in a region below the 3V (i.e., the optic chiasm) at onset (B) and peak disease (C). These hyper-intensities differed from the increased signals of the trigeminal nerves (arrows) in the T2W MRI of wild type (D) and sham control mice (E). The ventricles appeared enlarged at onset (B) and peak (C) EAE.

3.2.2 Hyper-intensities in ADC maps with EAE

Directional ADC maps represented ADC values calculated from a line of best fit to either four (N=35) or three diffusion-weighted images (N=13). ADC maps of experimental mice, diffusion scaled by colour (Figure 1), displayed greater intrinsic diffusion in the lateral and third ventricles (Figure 6). With EAE progression, additional pixels (POIs) displayed greater diffusion represented by increased signal intensities (hyper-intensities). As with T2W MRI, these hyper-intensities were localized in regions lateral and ventral of the third ventricle (i.e., lateral edges of the optic chiasm). Pathological changes, such as inflammation, edema and myelin and axonal damage [154-159] were considered responsible for the occurrence of EAE hyper-intensities (Figures 6E-L). Compatible with T2W MRI, the DWI-derived ADC maps indicated enlarged ventricles at onset (Figures 6E-L) and peak (Figures 6I-L) EAE.

Figure 6. Directional ADC maps of an EAE mouse.

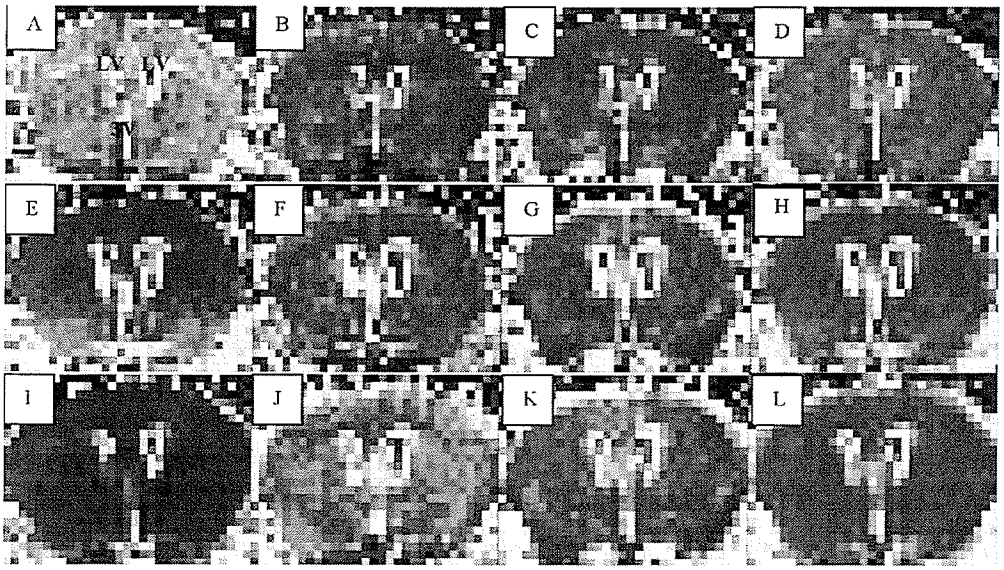

ADC_x (A, E, I), ADC_y (B, F, J), ADC_z (C, G, K) and ADC_{mean} (D, H, L) maps shown for the same EAE mouse at pre- (A-D), onset (E-H) and peak (I-L) disease. Normal anatomical regions of hyper-intensities included the lateral ventricles (LV) and the third ventricle (3V) (A). Additional hyper-intensities lateral and ventral of the 3V represented pathological changes with EAE progression within the optic chiasma (E-L). Enlarged ventricles were apparent at onset (E-J) and peak (I-L) disease. All ADC values were colour scaled as shown in Figure 1. Bar = 3 pixels = 939 μm (A).

The hyper-intense POIs that were visible at onset (Figure 7B) and peak (Figure 7C), were not observed in ADC maps of pre-disease (Figure 7A), wild type (Figure 7D), nor sham control (Figure 7E) mice. (Note: Figure 7 and Figure 5 show images from the same mice, ADC_{mean} maps and the T2W MR images, respectively. Results regarding the changes in directional diffusion will be addressed with statistical results in *Section 3.4*).

Figure 7. DWI-derived ADC_{mean} maps of C57BL/6 mice brains.

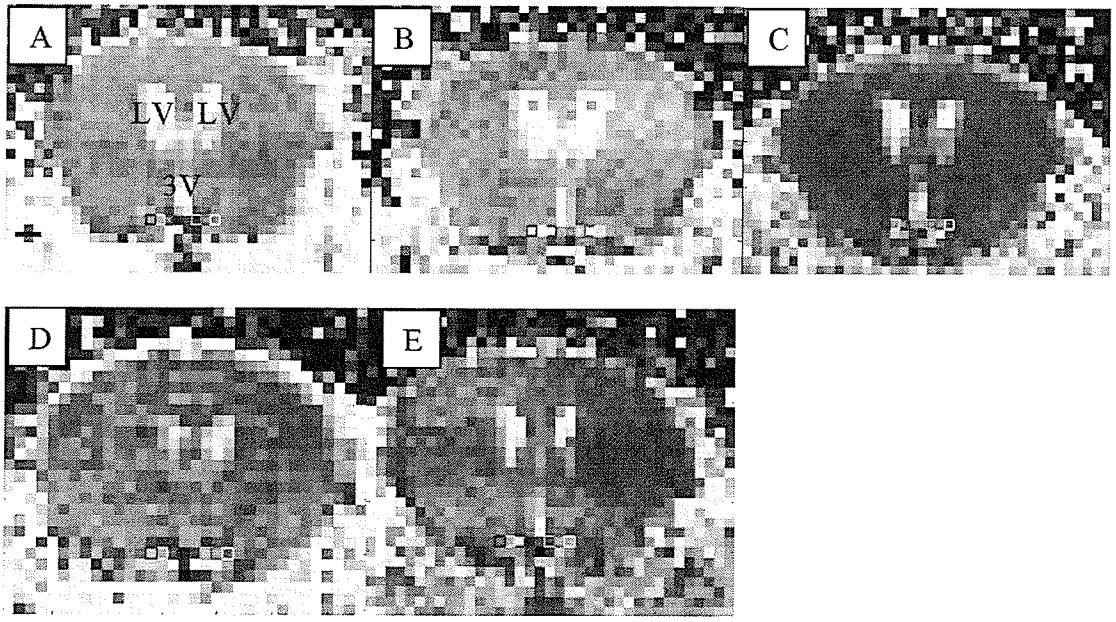

All ADC_{mean} maps included the normal anatomical regions of hyper-intensities: the lateral ventricles (LV) and the third ventricle (3V) as shown for pre-disease (A). Images of the EAE mouse at onset (B) and peak (C) contained pixels with increasing signal intensity lateral and/or ventral of the 3V with EAE progression. POI selections (i.e., six coloured boxes) represented row B. Based on the ADC scale (Figure 1), pre-disease (A) wild type (D) and sham control mice did not indicate increased diffusion in the region of the optic chiasm (i.e., POIs). Bar = 3 pixels = 939 μm (A).

3.3 EAE histology

HE (Figure 8A) and SC (Figure 8B) histology showed EAE pathology that corresponded with the MRI hyper-intensities. At 200x magnification, inflammatory aggregates were apparent on the lateral surfaces of the optic chiasm as highlighted in Figure 8A. The amount of myelin stained with SC in the optic chiasm of EAE mice appeared to be reduced at 40x magnification (Figure 8B).

Figure 8. Histological representation of the optic chiasm of an EAE mouse.

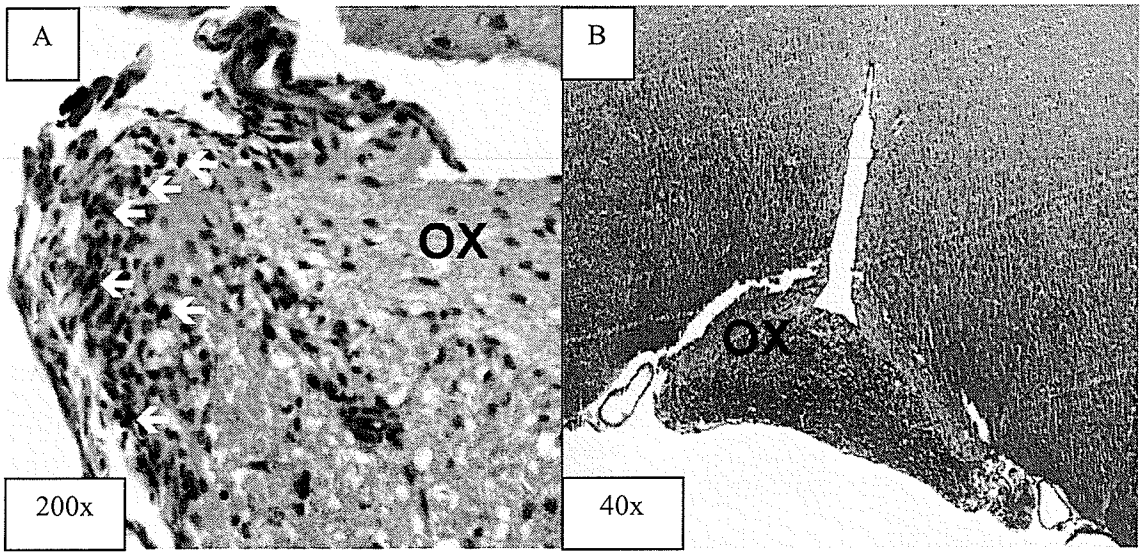

The pathological changes with EAE progression were examined with HE (A) and with SC (B). Inflammatory aggregates (arrows) and suspected myelin reduction (blue stain) were observed around the lateral regions and within the optic chiasm (OX). Photographs were taken at 200x (A) and 40x (B) magnifications.

Plastic embedded tissues were prepared for plastic section microscopy and EM examination as described in *Appendix F*. Semi-thin (0.5 μm) and thin (80 nm) sections of the optic chiasma of EAE (N=4) and control (sham controls N=2 and wild type controls N=2) C57BL/6 mice were evaluated. At the light microscopic level the wild type control optic chiasma consisted of densely packed myelinated axons with thin-walled blood vessels on the ventral surface. The EAE mice had intense inflammatory infiltrates on the surface especially around the blood vessels. Morphologically, the inflammatory cells included lymphocytes and neutrophils. Some inflammatory cells were identifiable within the chiasm, and the myelinated axons appeared separated because of edema. While no

photographs were taken, EM supported these visual observations (JEOL 1010 microscope) of semi-thin sections from the same tissue.

Thin sections showed no pathological abnormalities within the optic chiasma of wild type control mice (Figure 9A). The ventral surface of the optic chiasm and the presence of associated veins on the surface were visible. Myelin sheaths surrounded all but the smallest axons. At 8,000x magnification, no lymphocytic or mixed inflammation was apparent in the surrounding regions of the optic chiasm.

The optic chiasma obtained from mice that had developed mild EAE showed various signs of mixed inflammation concentrated at the lateral surface. Intense perivascular inflammation was evident on the chiasm surface that surrounded the blood vessels at 4,000x magnification (Figure 9C). To a lesser degree, lymphocytes, neutrophils and microglia invaded the chiasma. The degeneration of oligodendrocytes, myelin, and early axonal damage were also apparent. Chiasma thickness showed marked increase possibly because of the combination of abnormalities. These included inflammatory cell invasion, delamination of myelin (i.e., myelin was less tightly packed together), axon and cell swelling and increase in extracellular contents. Damaged axons that were swollen and partially denuded of myelin were evident at 6,000x magnification (Figure 9D). Differences in the severity of EAE pathology (i.e., inflammation) between the left and right divisions of the optic chiasm were noted (not shown).

Some myelin sheath vacuolation was seen in a sham control mouse at 8,000x magnification (Figure 9B). Observed in these sections were enlarged axons with some inflammation restricted to the chiasm surface. There were no obvious signs of invasive inflammation as seen with EAE, nor distinctive abnormal pathologies.

Figure 9. Optic chiasma of C57BL/6 mice as seen with EM.

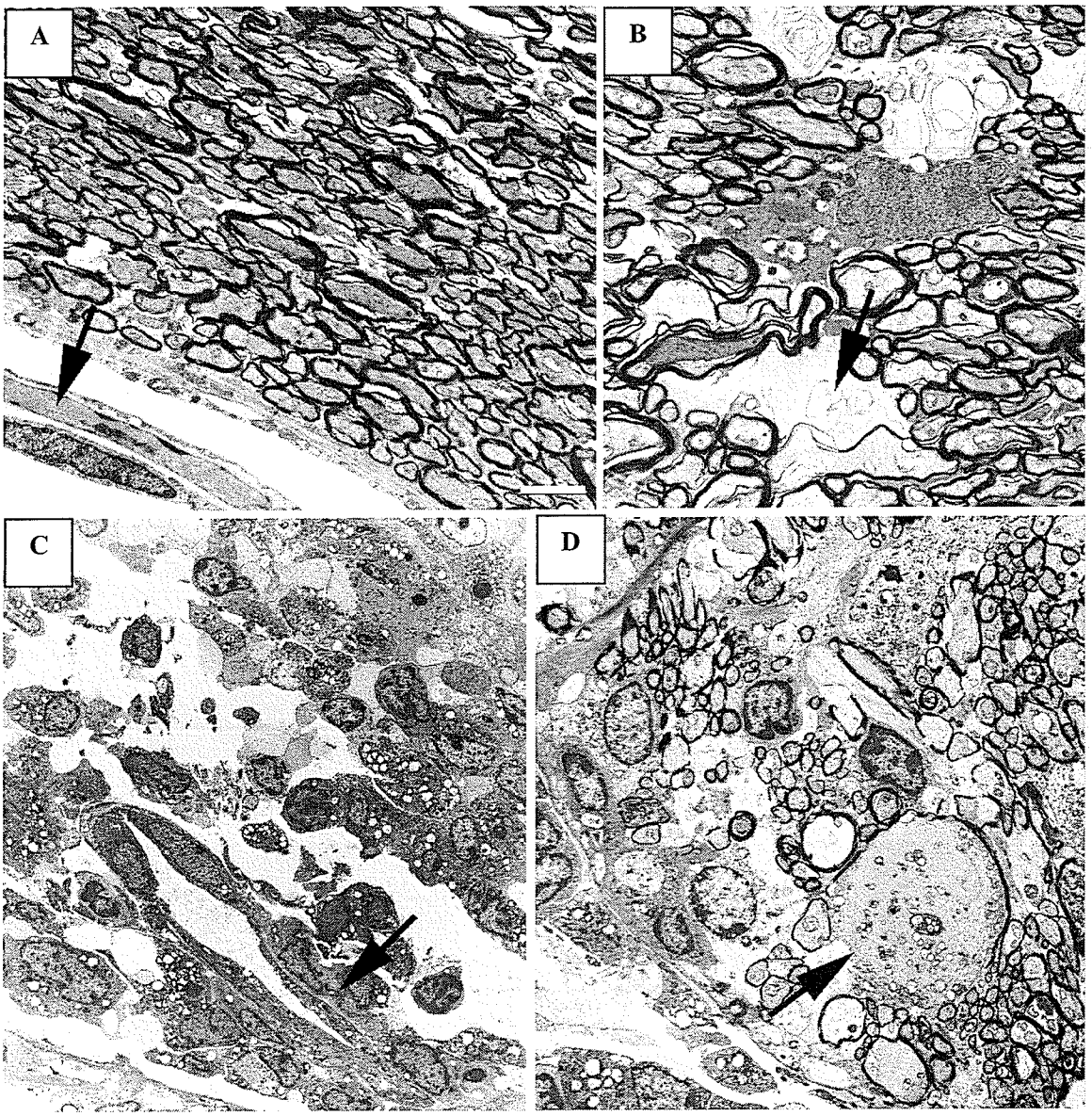

In wild type control mice (A) associated veins (arrow) were visible on the surface. The myelin sheaths surrounded all but the smallest axons. PTX inoculation (sham controls) was associated with some myelin sheath vacuolation (arrow, B). EAE was associated with intense perivascular inflammation on the chiasm surface surrounding the blood vessels (arrow, C). Lymphocytes and neutrophils invaded the chiasm. Damaged axons

were swollen and partially denuded of myelin (arrow, D). Bar = 2 μm (A). Photographs were taken at 8,000x (A and B), 4,000x (C) and 6,000x (D) magnification.

3.4 Statistical results

The one-way ANOVA measured between controls showed that none of the POI ADC values were significantly different. An example is shown in Figure 10. All anisotropies and comparisons between $ADC_{\perp}$ and ADC_z values showed non-significance with EAE (i.e., one-way ANOVA tests compared anisotropies and Student T-tests compared ADCs). These results are given in Table 5.

Figure 10. Row A POI ADC_{mean} values showed consistency between controls.

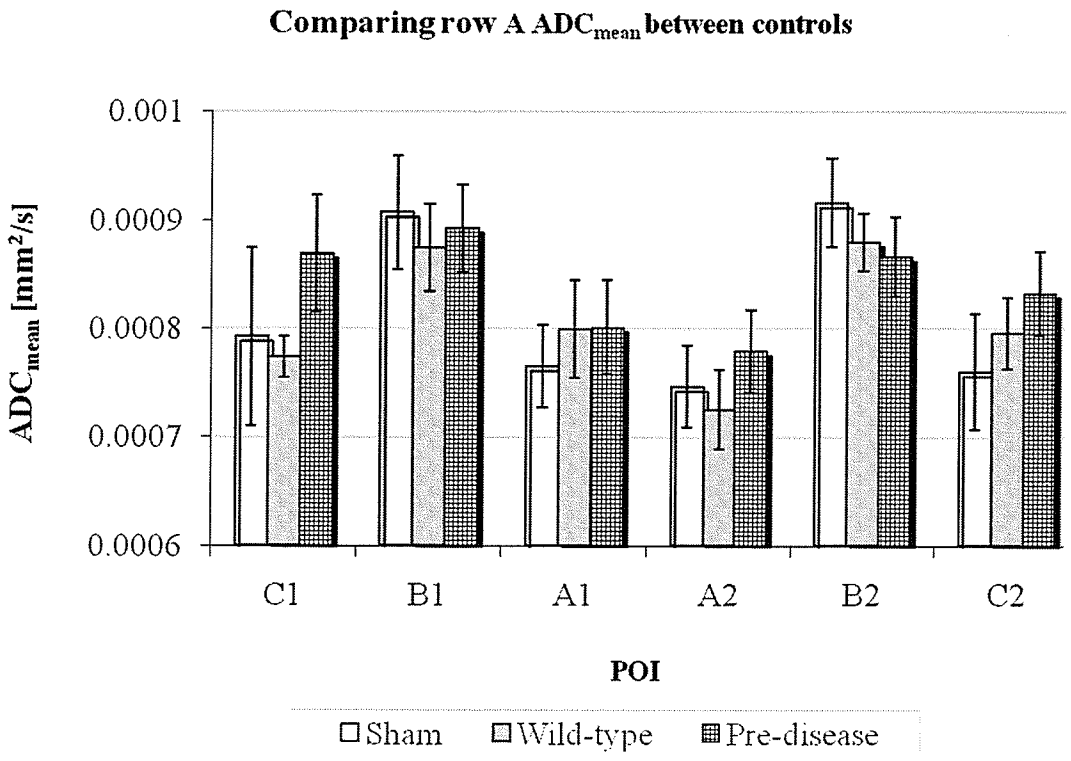

The mean ADC_{mean} values of individual row A POIs (i.e., C1 through C2) were compared by one-way ANOVA. No significant differences between controls ($p<0.05$) were indicated. The error bars represent the SEM.

Table 5. Mean $ADC_{\perp}$, ADC_Z and approximated anisotropies from all mice.

Study group per row	$ADC_{\perp}$ $[10^{-3}mm^2/s]$	ADC_Z $[10^{-3}mm^2/s]$	$ADC_Z/ADC_{\perp}$
Row A wild type	0.77 ± 0.04	0.89 ± 0.04	1.17 ± 0.04
Row B wild type	0.87 ± 0.07	1.09 ± 0.10	1.27 ± 0.07
Row A sham	0.80 ± 0.07	0.84 ± 0.08	1.05 ± 0.11
Row B sham	0.94 ± 0.13	1.13 ± 0.11	1.21 ± 0.09
Row A pre-disease	0.81 ± 0.05	0.90 ± 0.04	1.14 ± 0.06
Row B pre-disease	0.82 ± 0.07	1.09 ± 0.09	1.36 ± 0.09
Row A onset	0.87 ± 0.09	1.16 ±0.10	1.39 ± 0.12
Row B onset	1.18 ± 0.11	1.59 ± 0.13	1.36 ± 0.08
Row A peak	0.97 ± 0.11	1.16 ± 0.10	1.25 ± 0.10
Row B peak	1.11 ± 0.12	1.45 ± 0.14	1.34 ± 0.05

Mean $ADC_{\perp}$ and ADC_z values (Student T-test) and approximated anisotropies (one way ANOVA) did not measure significant differences.

3.4.1 Row A POI ADC values with EAE progression

Repeated measures ANOVA showed no significant differences in POI $ADC_{\perp}$ values (Figure 11A). However, there were significant differences in some POI ADC_z

(Figure 11B) and ADC_{mean} (Figure 11C) values. The Duncan's test showed that ADC_z values were significantly greater at onset disease compared to pre-disease in B1, A2 and C2. ADC_z values were also greater at peak in POIs A2 and C2. A2 ADC_{mean} was also significantly greater at peak compared to pre-disease. The significant changes in POI ADC values did not occur symmetrically with EAE. (P-values measured by Duncan's test are given throughout Figure 11).

Figure 11: Comparing row A POI ADC values with EAE progression.

A.

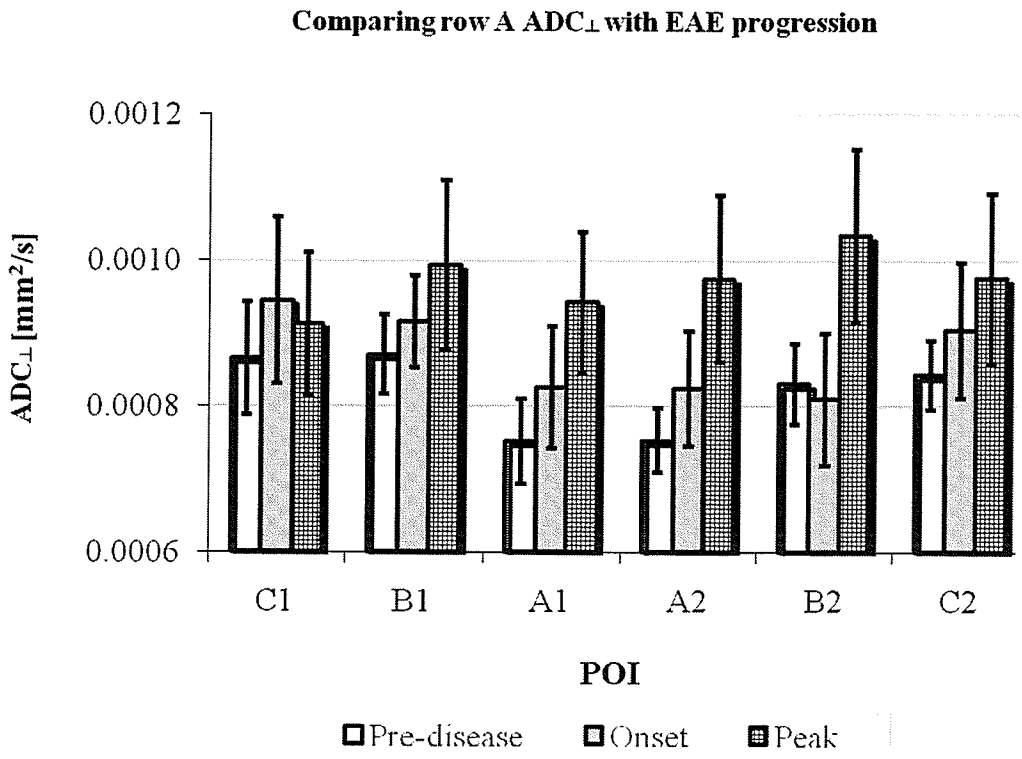

B.

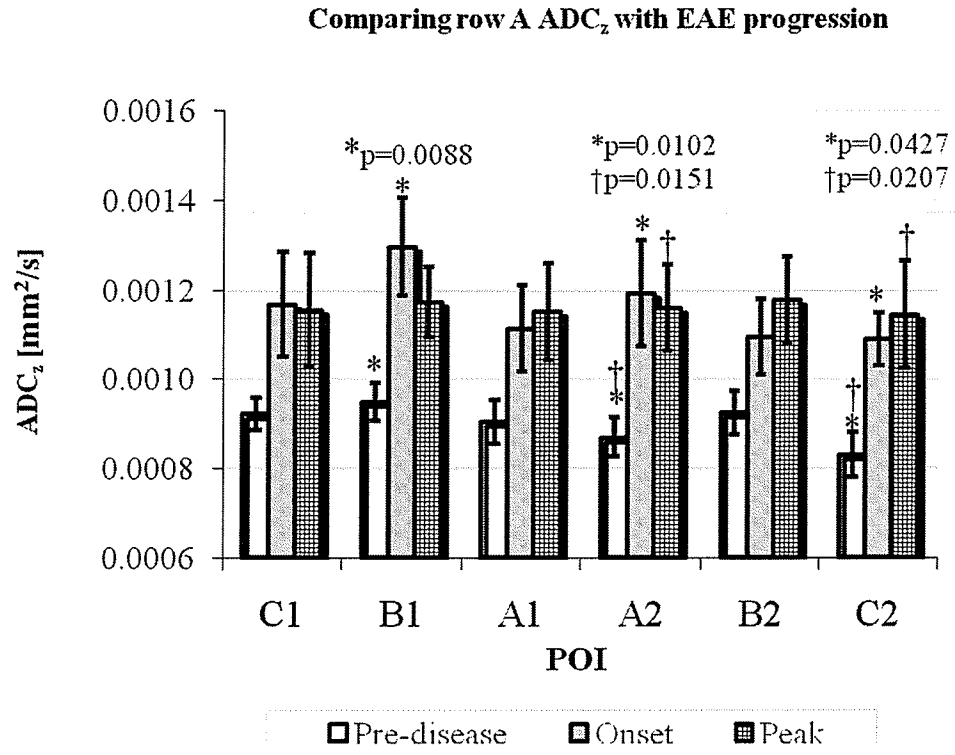
Comparing row A ADCz with EAE progression
0.0016
0.0014
0.0012
0.0010
0.0008
0.0006
ADCz [mm2/s]
*p=0.0088
*p=0.0102
†p=0.0151
*p=0.0427
†p=0.0207
C1
B1
A1
A2
B2
C2
POI
Pre-disease
Onset
Peak

C.

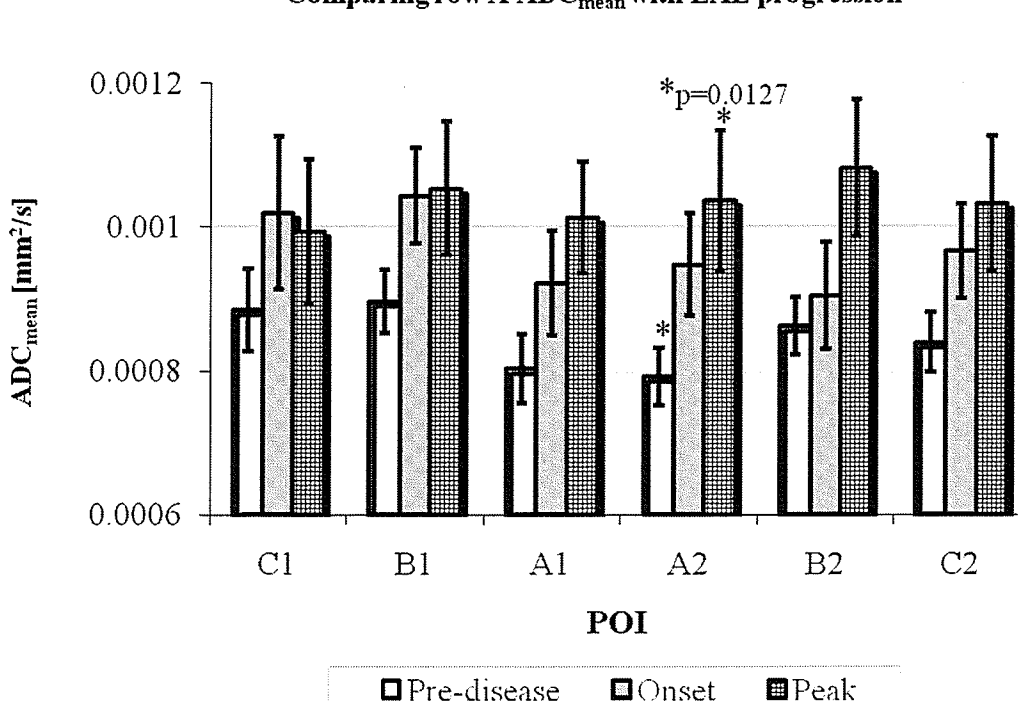
Comparing row A ADCmean with EAE progression
0.0012
0.001
0.0008
0.0006
ADCmean [mm2/s]
*p=0.0127
C1
B1
A1
A2
B2
C2
POI
Pre-disease
Onset
Peak

Repeated measures ANOVA showed no significant differences in POI $ADC_{\perp}$ values (A). ADC_z (B) and ADC_{mean} (C) values were significantly greater at onset and/or at peak in the POIs indicated (* and †). Statistically significant p-values (<0.05) were measured by Duncan's test. The error bars represent the SEM.

3.4.2 Row B POI ADC values with EAE progression

Repeated measures ANOVA showed significant differences in POI $ADC_{\perp}$ (Figure 12A), ADC_z (Figure 12B) and ADC_{mean} (Figure 12C) values. The Duncan's test showed that the $ADC_{\perp}$ values were greater at onset as compared to pre-disease in all POIs except C1 and C2. $ADC_{\perp}$ values were also greater at peak as compared to pre-disease in B1, A2 and B2. All but A1 and C2 POI ADC_z values were significantly greater at both onset and peak as compared to pre-disease. A1 and C2 POI ADC_z values showed significantly greater ADC_z values at onset and peak, respectively. All but C2 POI ADC_{mean} values were significantly greater at onset as compared to pre-disease. POIs B1, A1, A2 and B2 also showed significantly greater ADC_{mean} values at peak. More pixels in row B had significant changes in ADC values with disease than in row A. Changes in row B ADC values were not symmetrical. (P-values measured by Duncan's test are given throughout Figure 12).

Figure 12: Comparing row B POI ADC values with EAE progression.

A.

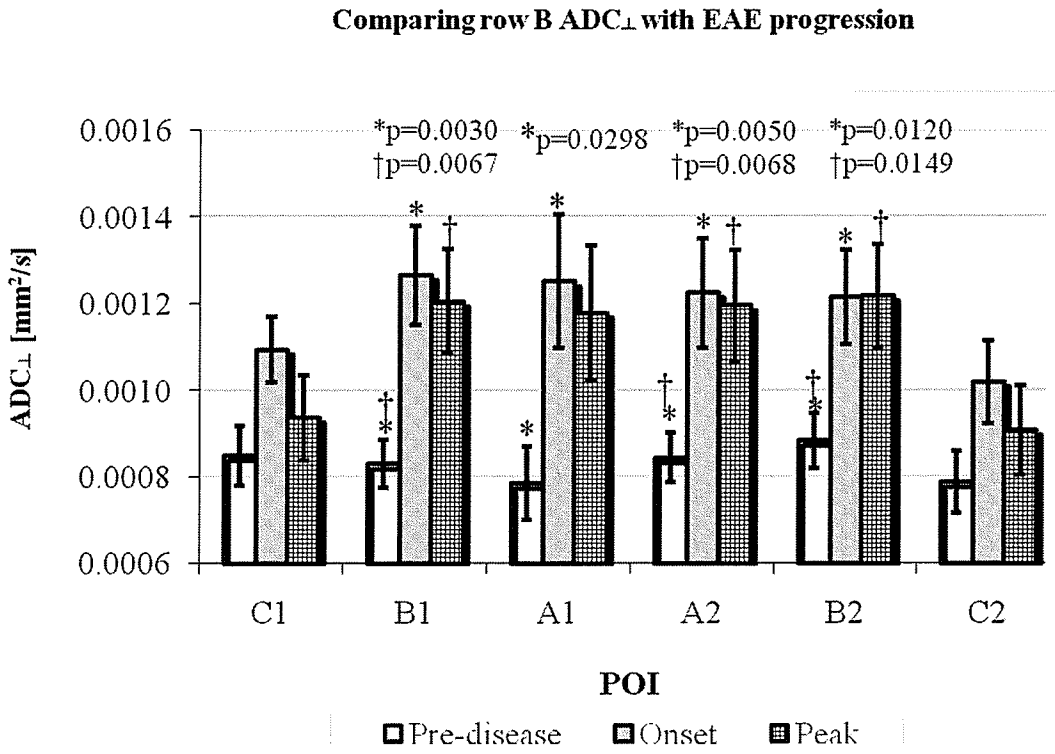

B.

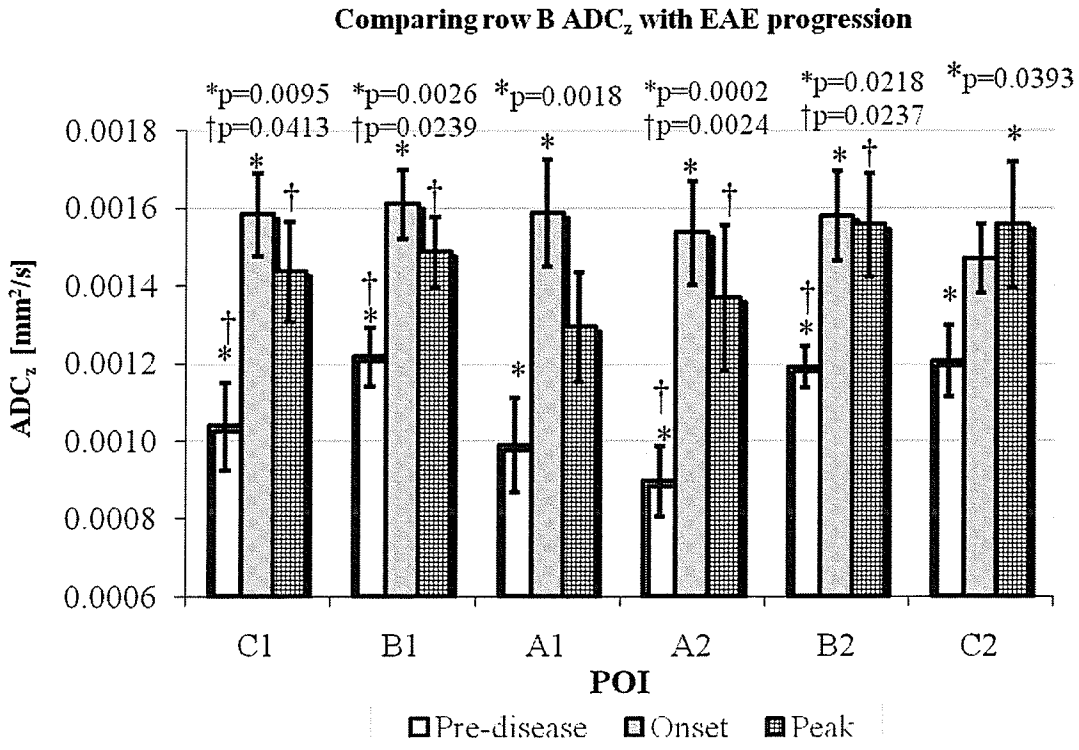

C.

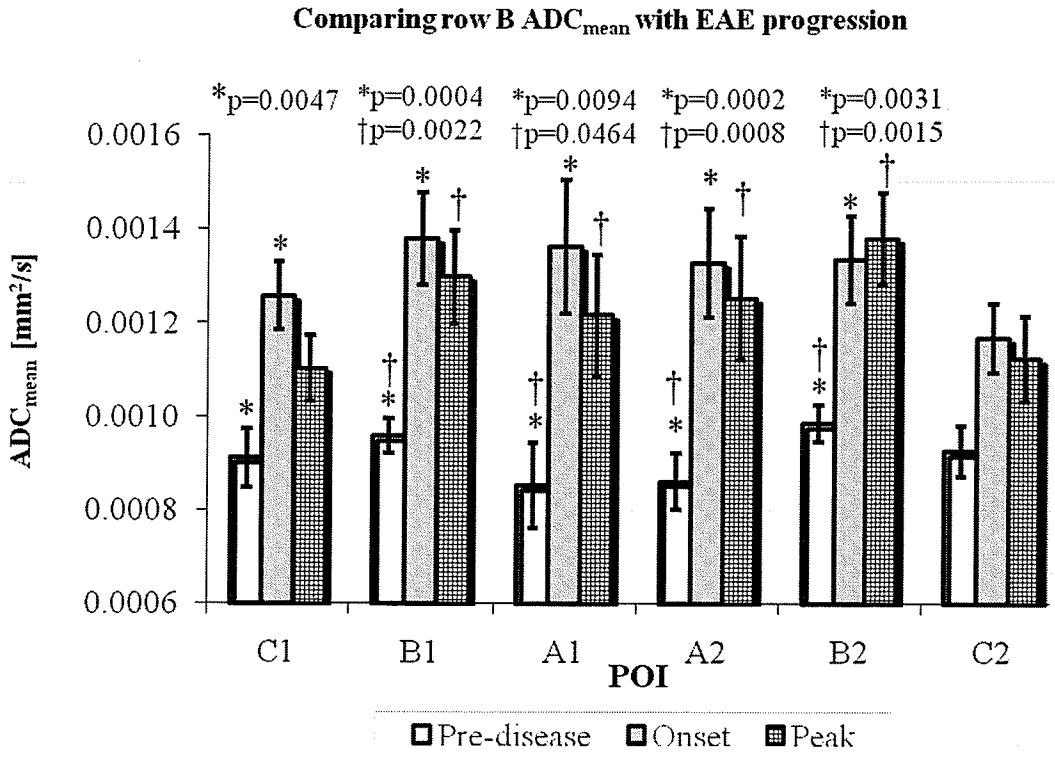

Repeated measures ANOVA showed significantly greater $ADC_{\perp}$ values (A), ADC_z (B) and ADC_{mean} (C) values at onset and/or at peak in the POIs indicated (* and †) as compared to pre-disease. Statistically significant p-values were measured by Duncan's test. The error bars represent the SEM.

CHAPTER 4: Discussion

4.1 EAE in the optic chiasm

Following MOG_{35-55} induction (N=39), C57BL/6 mice (N=23) developed EAE (Table 4). EAE mice showed a correlation between the change in clinical score and the decrease in body weight (Figure 3), which has already been described [108,174,184,185]. As the severity of disease increased, body weight decreased. The weight increase prior to EAE was expected for C57BL/6 mice of this age from Charles River. Even after 11 weeks, normal C56BL/6 mice experienced steady increase in body weight [186].

MOG_{35-55} immunization presented mild monophasic EAE. T2W MRI (Figure 5) and DWI (Figure 6 and Figures 7A-C) identified lesions in the optic chiasm. Recall that the optic chiasm was selected for study because recent studies reported inflammation, demyelination, axonal injury and ON in EAE mice [108,111,112,119]. Additionally, the severity of EAE insults was greater in the optic chiasm compared to the spinal cord [119]. EAE with ON might be considered an early MS model because ON is often an early sign of MS [18]. In this thesis, increased signal intensities were localized in POIs adjacent to and/or below the third ventricle. Significant increases in ADC values were considered consequences of EAE pathology along the lateral edges of the optic chiasm.

As compared to wild type controls (Figure 9A), histology confirmed varying degrees of inflammation, edema, axons denuded of myelin, and axonal damage in the optic chiasm of EAE mice (Figure 9D). Inflammation was shown on the chiasm surface surrounding the blood vessels (Figure 9C). Inflammation and demyelination have already been characterized in MOG_{35-55}-immunized EAE mice [108]. In fact, previous

studies found similar EAE pathologies as described in this thesis within the optic nerves [108,111,112,119] and optic chiasma [187-190]. Typically, inflammation was concentrated in and around the subarachnoid blood vessels of the optic nerve and chiasm as seen in the EAE mice of this thesis (Figure 9C). More recently, axonal injury was described with ON in EAE mice [111]. In comparison, EAE effects on the axons were milder in the mice of this thesis. Although the success rate of induction in studies presented in this thesis was less than the anticipated 100% (*Section 3.1* and *Appendix A*), EAE displayed detrimental effects on the optic chiasm.

In the past, in the lab in which the thesis experiments were performed, similar (i.e., species, strain, age and sex) induction with MOG_{35-55} peptide and adjuvants had greater incidence of EAE (i.e., up to 86%) [174]. Protocols that differed either in dose (of MOG_{35-55} and/or adjuvant) and/or in injection methods have reported 85 to 100% incidence of EAE [78,88,108,187,191]. Although this variability in the success of EAE inductions has been noted, the causes were unknown.

Possible explanations for low incidence of EAE in the experiments presented in this thesis might be explained by poor emulsification (i.e., MOG_{35-55} and CFA suspension), poor PTX and/or MOG_{35-55} injections [182]. The season at the time of induction displayed no correlation with the incidence of EAE disease (*Appendix A*) unlike what was reported by Teuscher et al [192]. While Teuscher et al showed increased susceptibility for EAE induction in summer months (July through September), our results did not show this trend perhaps because different strains were studied. Insufficient (MOG_{35-55} specific) T cell priming was another suggested source for low EAE success

[88,193]. In fact, studies that reported 100% incidence included a booster immunization of MOG_{35-55}.

To our knowledge, sham controls presented histopathology that has never been described in mice inoculated with only PTX. Inflammation restricted to the chiasm surface, myelin sheath vacuolation and enlarged axons were observed (Figure 9B). Previous studies reported no breakdown of the BBB [194], nor any clinical and/or histological occurrences of ON and/or EAE [87]. Mice that were inoculated with both PTX and CFA also showed no changes in the integrity of the blood-spinal cord barrier [174]. An alternative study that prompted the inclusion of the sham controls for this thesis, measured irregular delayed VEPs in their sham controls [178]. Delayed potentials were considered indications of inflammation and/or altered myelin integrity, which were mildly observed in the optic chiasm of sham controls (Figure 9C). While previous studies proved that the brain and spine were unaffected by PTX inoculation, our histology (in addition to the irregular VEPs) suggested that PTX might have mildly influenced the optic chiasm.

4.2 T2W hyper-intensities correlate with EAE

WM T2W lesions of EAE mice (Figures 5B and C) might be related to any of the pathological changes observed in the optic chiasma (Figures 9C and D). While T2W lesion detection has already been recognized [130-133], there were no lesion differentiations [135,136]. T2W MRI was performed to easily verify lesion presence, to position the slice, and (in this higher resolution image) to successfully include the optic chiasm for (the lower resolution) DWI.

T2W hyper-intensities in EAE mice were localized in a region lateral and ventral to the third ventricle (Figures 5B and C). This was not surprising because EM confirmed the pathological effects of EAE in this region (Figures 9C and D). Hyper-intensities as described for EAE mice were not observed in T2W MR images of pre-disease (Figure 5A), wild type (Figure 5D) and sham control (Figure 5E) mice. Despite the mild EAE histopathology in the optic chiasm of the latter control group (Figure 9B), no T2W lesions were observed with T2W MRI (Figure 5E). T2W MRI might have been insensitive to the minute degree of inflammation and changes in myelin and axon in sham controls (perhaps because of the limited spatial resolution).

Recall that some non-EAE images included small regions of increased signal that were less proximal to the third ventricle (Figures 5D and E). Marked by the difference in size and location, these additional signals were considered attributes of the surrounding trigeminal nerves (*Section 3.2.1*). Signals from the trigeminal nerves could be detected if the orientation of the diffusion-sensitive gradients and the direction of the axonal tracts were not perfectly aligned [195]. However, this non-mutual coherence between the direction of the axonal tracts and the diffusion-sensitive gradients has little relevance to T2W MRI. It is unclear whether the large size of the trigeminal nerves attributed to the increased signal observed in the non-EAE mice (Figures 5D and E).

No quantitative analysis of T2W images was performed because T2W MRI was unable to provide lesion specificity. Instead, mice were further investigated with DWI and ADC values (i.e., $ADC_{\perp}$, $ADC_{\parallel}$ values and ADC_{mean}) were measured in the optic chiasm to test their utility as possible surrogate markers for myelin and axonal damage.

4.3 ADC values were consistent amongst controls

As expected (because no pathological differences were suspected amongst control mice), no significant differences in POI ADC values were measured between controls (Figure 10). EM confirmed that no pathological changes occurred in wild type controls over time (Figure 9A). While mild pathologies were observed in the sham control mouse (Figure 9B), ADC values were not significantly different. Perhaps the degree of PTX effects on the optic chiasm was insignificant for DWI (similar to T2W MRI results) because of non-optimal resolution. Reduced sensitivity for pathological changes might have also occurred from using DWI rather than DTI for ADC calculations. Both these limitations could be unbound by improved hardware and software of the Bruker Biospec spectrometer itself (*Section 4.5*). In any case, consistent ADC values (i.e., non-significantly different) proposed that no EAE pathologies occurred. The histopathology of pre-disease mice was not studied because the terminal end-point was peak EAE. However, the MRI of pre-disease mice was performed early after immunization. ADCs measured at pre-disease were considered unaffected by EAE because no significance was measured in ADC values of pre-disease and wild type controls.

4.4 ADC values increased with EAE

Despite the non-significant changes in $ADC_{\perp}$ values of row A POIs, ADC_z and ADC_{mean} values significantly increased with EAE (Figure 11). ADC values obtained from row B POIs also increased with EAE (Figure 12). The increases in the ADC values of both rows indicated tissue changes at the lateral edges of the optic chiasm. Based on

the experimental observations, the support for ADCs as plausible markers for specific pathologies were as follows:

A) While myelin integrity proved to be compromised with EAE, significant increases in $ADC_{\perp}$ values were restricted to row B POIs. Shredded and/or thinned myelin in the optic chiasm (Figure 8D) might have imposed fewer boundaries in the perpendicular direction and contributed to the increased $ADC_{\perp}$ values (Figure 12A) [154-158].

B) Both rows measured significant increases in ADC_z values with EAE (Figures 11B and 12B). However, only reduced longitudinal diffusivities were previously reported as plausible markers for axonal injury [112,160] rather than increased $ADC_{\parallel}$ values. Any decreasing effect on ADC_z could have been overwhelmed by pathologies that might have increased diffusivity. In other words, edema, inflammation and/or demyelination (Figures 9C and D) might have dominated the change in ADC_z values as opposed to axonal injury.

C) While increases in ADC_{mean} were minimal in row A (Figure 11C), increased ADC_{mean} values (with EAE) were prominently measured in row B POIs (Figure 12C). Increased ADC_{mean} might have resulted from various pathologies that were confirmed with EM. Putative pathologies were surface and invasive inflammation, edema, and early myelin damage (Figure 8 and Figures 9C and D).

Overall, both rows suggest that increasing ADC values are indicative of the EAE pathologies at the lateral edges of the optic chiasm. While a simple translation of the increasing ADC values with the resulting histopathology can provide support for myelin damage and inflammation, the effects of EAE on the directional and mean ADC values

might actually be more complex. Before further elaboration of the changes expressed by ADCs, the potential sources of errors in ADC calculations should be addressed.

4.5 Potential sources of errors

The potential of the Bruker Biospec spectrometer might have affected the accuracy of ADC calculations. At the time of the imaging, the hardware and software limitations might have contributed to partial volume effects, eddy current effects and image noise. Additionally, the limited Bruker Biospec spectrometer potential prevented the application of additional b-values and the application of the more sophisticated DTI MRI. Further errors might have resulted from sources independent of the Bruker Biospec spectrometer abilities such as motion, temperature variations and position of the live mouse.

One recurring product of the gradient potential is the limited resolution of DWI (312.5 x 312.5 x 1,000 μm^3). DWI of the small optic chiasm (approximately 1.0 ± 0.25 mm) [181] at low resolution is difficult because of the consequential partial volume effects. The ADC becomes a more macroscopic representation of diffusion at lower resolution because of the larger pixel/voxel size.

At the given resolution, the optic chiasm of a normal mouse should be represented by 2.4 to 4 pixels. The difference between the actual size of the optic chiasm and the resolution of DWI allowed a particular pixel to contain more than one type tissue. The accuracy in ADC calculations was then compromised. To account for all of the areas that were affected by EAE, POI selection included the lateral ends of the optic chiasm and the surrounding regions where increased diffusion was apparent (*Section 2.4.3*). This

selection resulted in a single segmented row (Figure 1). Recall that ADC values were measured from two rows (A and B) to also make up for any partial volume error(s) along the superior-inferior line. Rather than accounting for partial volumes with POI selection, its elimination by improving image resolution would have been more ideal (i.e., by making pixels/voxels less macroscopic). However, maximizing image resolution to reduce partial volumes required smaller FOVs and increased matrix sizes [196]. This could only have occurred (with the same Bruker Biospec spectrometer) by gradient upgrades.

Eddy currents might have occurred as a result of gradient coils that were switched quickly as part of the routine DWI sequence [197]. The resultant differences in field gradients between those experienced at the sample and that prescribed by the pulse program for the diffusion weighting would then have affected the accuracy of ADC calculations. In addition, MR images would have been distorted if there were slowly decaying eddy currents during the readout period. Improved gradients with better software would have automatically corrected for the presence of eddy currents. However, at the time of the imaging, the best solution was to first try complementary b-value images. If the combination did not suffice, then defected images were discarded and ADC data was refitted with three b-value images rather than four (*Section 2.4.2*).

Unwanted image noise that can result from both MR hardware and the subject of interest also affects ADC calculations. As the diffusion weighting (i.e., b-value) increases, the signal decreases exponentially. Eventually, the signal level gets closer to the noise threshold and causes errors in the ADC calculations. While the increase in B_o from clinical scanners or maximization in NEX can improve SNR (*Sections 2.3 and*

2.3.2), a baseline 'noise floor' can ensue [197]. Further noise reduction can only occur with upgrades on both the hardware and the software.

Based on the abilities of the Bruker Biospec spectrometer, the inclusion of additional b-values to improve the line of best-fit data and therefore improve ADC calculations was not applied. Additional b-value images would have produced longer scan times. In the end, each scan would have been more susceptible for motion artifacts and possibilities of mechanical errors (i.e., drifting).

During the scan times of this thesis, animals were anaesthetized to minimize movement. Nonetheless, even minute motions (i.e., breathing and mouse moving its head out of the holder) could have produced image artifacts. Such possible artifacts could have included spatial blurring and misregistration (i.e., the brain shifting positions between images). While shorter scan times (restrained by the abilities of the Bruker Biospec spectrometer) would have reduced susceptibilities for motion artifacts, any that had occurred were resolved by image registration (*Section 2.4.1*).

Because diffusion is temperature dependent, varying temperatures can also potentially affect ADC calculations. While the exact relationship between temperature and diffusion within a biological system remains unknown, the increase in temperature increases the free diffusion. Holz and colleagues best fitted their data to a Speedy-Angell power law [198,199]. Recall that temperatures were maintained at best between 36.5 and 38^0 C (*Section 2.3*). According to the Speedy-Angell plot, the corresponding temperature dependent free diffusivities would be $3.004 - 3.103 \times 10^{-3}$ mm^2/s. Supposing that the effect of temperature is similar on the diffusion of water in biological tissues, greater ranges might have greater effects on the diffusion weighting and affect the final

measurements of ADCs. For this reason, temperatures during MRI were monitored frequently.

The correct position of the mouse was necessitated for two reasons. Proper positioning of the brain was required to accurately represent the ADC values of the optic chiasm. Secondly, coherence between the orientations of the axonal tracts and the diffusion-sensitive gradients (in the z-direction) was anticipated to reduce inaccuracies in approximating $ADC_{\perp}$ and $ADC_{\parallel}$ values.

The more sophisticated DTI would have accurately calculated $ADC_{\parallel}$ and $ADC_{\perp}$ rather than making approximations from ADC_z, ADC_x and ADC_y (regardless of the position of the animal). However, *in vivo* DTI was not applied because of the hardware limitations. While DWI experiments in this thesis used three diffusion directions, DTI required at least seven. Without upgrades on the Bruker Biospec spectrometer, the scan-time would have more than doubled. Mice would have required further anaesthetics, which could have resulted in death at later stages of EAE. Furthermore, the image would have been more susceptible to hardware and motion artifacts. Given these constraints, ADC values were calculated via DWI with low spatial resolution.

4.6 Interpretation of ADC increases

The inherent crossing of axons in the optic chiasm should be considered in the interpretation of the ADC results. An axon originating from the left optic nerve can cross at the chiasm and pass to the contralateral optic tract. Even the axons that do not cross to the contralateral side approach the midline rather than traversing laterally throughout the chiasm. The crossing of axons in the mouse lends to the reduced order of longitudinal

orientation [200,201] and therefore complicates the assigning of one longitudinal direction to the optic chiasm.

Recall that any non-coherence between the orientations of the axonal tract and diffusion-sensitizing gradients might have affected the accuracy in ADC calculations with DWI [195]. Nonetheless, the optic chiasm was chosen for study for many reasons (*Section 4.1*). One of the reasons for selection was the large surface area (of the optic chiasm) relative to the resolution potential of the Bruker Biospec spectrometer.

While $ADC_{\perp}$ significantly increased and myelin damage was observed, studies [168,195,202] implied that it is naïve to reproach the increasing $ADC_{\perp}$ values on myelin damage alone. Even normally non-myelinated nerves possessed water diffusion that was significantly anisotropic and thus myelin was not considered the only constituent for anisotropy [203]. Also, ADC values of the non-myelinated optic nerves of Jimpy mice and those of normal controls were not significantly different [195]. Diffusion anisotropy was also evident in a human study of hypomyelination [202]. Together, both these results suggested that the diffusion anisotropy was not exclusive to the multiple layers of the myelin sheath. Considering the crossing axons in the optic chiasm, increased $ADC_{\perp}$ values appeared much more complicated than the boundaries of diffusion set by the myelin sheath.

Interestingly, the mean anisotropy in each study group (Table 5) was less than the reported anisotropies for the optic nerves and tracts (approximately two to four) [112,154,155,195]. The calculated anisotropies seemed to be attributed to the smaller ADC_z values (Table 5) than the reported $ADC_{||}$ values (i.e., 1.41 to 1.79 x 10^{-3} mm^2/s) [112,154,195]. This difference (in the ADC_z and $ADC_{||}$ values) was first considered

erroneous and the cause of low-level anisotropies. Reasons first considered for the low-level ADC_z values were:

A) The mouse was not positioned in such a condition that axons were aligned directly longitudinal to the z-gradient, and/or

B) The POI(s) did not contain only the optic chiasm (i.e., partial volume effect).

But even if these were always the case, the following question still remained. *Which pathological features caused the $ADC_\perp$ and ADC_z values to increase (yet remained lower than reported for the optic nerve) in the EAE chiasma*?

The less anisotropic diffusion in the optic chiasm of wild type control mice (than in the optic nerve and/or tract) might be attributed to the reduced order of (longitudinal) axons in the optic chiasm [200,201]. Contrary to the chiasm, the axons ran parallel throughout the course of the optic nerves and tracts. Perhaps diffusion in the chiasm was bounded in all directions in approximately equal amounts because of the crossing axons. The mean anisotropy calculated for wild type controls was indeed approximately equivalent to the value of one (i.e., diffusion was not really anisotropic). This was true for each study group (Table 5).

From mathematical reasoning, the anisotropy cannot remain unchanged if only one of the directional diffusivities increased significantly (e.g., $ADC_\perp$). In fact, both $ADC_\perp$ and ADC_z values increased significantly with EAE progression (Figure 11C and Figures 12A and B) while the degree of anisotropy seemed relatively consistent (Table 5). This suggested that the thinning and shredding of myelin in the optic chiasm might have actually reduced the hindrance on diffusion in all directions and not exclusively in the orthogonal direction.

Reasons for increasing ADC_z values exclusively were less intuitive because previous studies reported only decreased ADC_z values with axonal injury (i.e., in nerves where the ordered axons were running approximately parallel to the z-direction). In the condition where ADC_z values increased (in normal developing mice) [195] the axons conformed from a tortuous to straight manner. This conformation in shape might be related to myelin development. Given the axonal crossovers in the chiasm, perhaps both the myelin and axonal damage that occurred in the EAE mice (of this thesis) contributed to a straighter path of diffusion. EAE processes might have reduced diffusion barriers and therefore allowed significantly increased ADC_z values.

Given that both $ADC_\perp$ and ADC_z values were significantly increased with EAE (Figure 11B and Figures 12A and B), the increase in ADC_{mean} values was expected. Changes in mean diffusivity have been linked less specifically to pathological changes [163]. Analogous to T2W lesions that appeared with inflammation, edema, demyelination and axonal damage, ADC_{mean} lesions lacked lesion specificity [159,164]. Therefore, the increased ADC_{mean} values that occurred with EAE (Figure 11C and Figure 12C) only confirmed that pathological changes existed in (both rows of) the POIs. These changes could have been indications of any or all of the effects of EAE (Figure 8 and Figures 9C and D) except axonal damage that is known to decrease $ADC_\parallel$ values [112,156,159,160].

Vasogenic edema that is associated with inflammation has also been linked to reduced anisotropy [166,167] and increased ADC values [165]. With EAE, the changes in approximated anisotropies were non-significant (Table 5) and yet the ADC values increased (Figures 11B and C and Figure 12). One EAE study [204] explained that the

increased diffusivities in three directions were attributed by the freely diffusible water in the acute inflammatory build-up. It could be possible that the increased water diffusion near the chiasm surface where inflammation was predominant (Figure 8A and Figure 9C) contributed to the increase in ADC values.

Despite the loss of accuracy in ADC calculations and the inherent crossing of axons in the optic chiasm, DWI measured significant differences in EAE mice. Both EM and ADC results suggested that the severity of EAE was non-symmetrical in the optic chiasm. Additionally, the degree of anisotropy in the optic chiasm of all mice was measured to be less than the reported anisotropies for the optic nerve and/or tract (Table 5). Directional ADC values increased with EAE (Figures 11 and 12) and might have included information about myelin and axonal injury, and about inflammatory exudates. All of the pathological changes might have cooperated in the chiasm and increased diffusion in all directions (and had little impact on the anisotropy). DWI quantified changes in the optic chiasm of EAE mice and the presence of pathological changes was confirmed by histology. The results supported a relationship between ADC changes and EAE pathologies within the optic chiasm.

CHAPTER 5: Conclusion

5.1 Future work

The experiments of this thesis were carried out to investigate MOG_{35-55}-immunized EAE lesions in the optic chiasm by quantitative imaging methods. The diffusivities (i.e., $ADC_{\perp}$, ADC_z and ADC_{mean}) were tested as putative surrogate markers for myelin and axonal injury, and for inflammation and/or edema. Perhaps due to the structural order of axons in the optic chiasm, some unexpected results occurred. Namely, the degree of anisotropy was less than that reported for other WM structures and did not significantly change with EAE. $ADC_{\perp}$ and ADC_z values were however significantly increased with EAE progression. These increases reflected pathological changes, which were confirmed by histology.

One interesting outcome includes the results of sham control (i.e., PTX inoculated) mice. Recall that the EM of sham control mice showed surface inflammation and myelin vacuolation. No analogous studies to our knowledge had similar observations. However, no MRI hyper-intensities (i.e., with T2W MRI and DWI that would have supported the histopathology of sham controls) were detected.

Based on the results of PTX on the optic chiasm and its possible influence on VEPs [178], a less invasive model might be more suitable for future studies. The MOG-specific TCR transgenic mouse model that spontaneously develops ON and EAE [87] might provide lesions in the optic chiasm that are definite disease pathologies and eliminate the possible effects of adjuvants. An additional benefit of this model is the high frequency of histological ON that can occur without EAE.

What lies ahead are studies with improved imaging hardware and software that would provide higher resolutions and thereby reduce partial volume effects. This would allow more reliable ADC calculations. In a perfect experiment, one could address all of the sources of errors (*Section 4.5*) to ensure the accuracy of ADC values. Future upgrades on the Bruker Biospec spectrometer such as improved shim and gradient coils in addition to new controls software, could allow DTI to be performed in minutes (as compared to hours). These studies might offer more specificity to the pathological disruptions on the optic chiasm that was observed in this thesis.

Recall that MRI results of EAE mice also showed enlarged ventricles (Figures 5B and C and Figures 6E-L), which have already been identified in EAE [205]. Quantification and histology of the enlarged ventricles were not performed because this thesis was primarily interested in the pathology within the optic chiasm. Future work could implement both the above-mentioned processes for validation.

While clinical manifestation and spinal chord lesions have reported symmetrical insults [206,207], the severity of EAE (i.e., levels of inflammation) between the left and right sides of the chiasm suggested differences. Subsequently, changes in ADC values were not entirely symmetrical. These results might be explained by the common unilateral (compared to bilateral) occurrence of ON [16]. However, more meticulous investigations should be performed to substantiate these findings. Improved spatial resolutions and the addition of correlating histopathology and ADC values specifically from the left and right divisions of the optic chiasm could be applied.

Future work could also implement two additional data sets by investigating the optic chiasm when the weight loss precedes EAE and from MOG_{35-55}-immunized mice

that do not develop (clinical) EAE. The data from both these conditions might contain useful information about MOG_{35-55} effects on the optic chiasm and its relation to motor deficits. VEP testing in addition to MRI and histology could further provide a robust method to investigate these optic lesions.

This pilot study can pave the way for vast research opportunities in pharmacology. Not only could one confirm directional changes in ADCs as robust biological markers for WM diseases, improved methods could provide a basis for longitudinal drug studies (i.e., useful for human WM diseases such as MS). Future VEP testing with MRI might provide alternative correlations and reduce the need for invasive histology. Along with stringent methodologies that will include additional data sets, future studies might be able to include tests that do not rely on motor impairment but are more specific for CNS effects (i.e., visual disturbances).

5.2 Closing

This study showed that MOG_{35-55}-immunized EAE mice experienced pathological changes in the optic chiasm. EAE results were observed with MRI and EM. Diffusion anisotropy in WM proved to be complex in the optic chiasm. The inherent crossing of axons might have further interfered with free water diffusion (in addition to the myelin sheath). While the anisotropy remained relatively consistent with EAE progression, the directional ADCs showed significant increases. These results suggested a plausible relationship with WM pathologies. However, the recurrent debate regarding changes in directional ADC values (i.e., $ADC_{\perp}$ and $ADC_{\parallel}$) as distinct surrogate markers for WM disruptions has yet to be settled. Nonetheless, these experiments showed that DWI ADC

maps were indeed sensitive to some EAE changes and provided a means for non-invasive lesion specificity for future studies.

REFERENCES

[1] Compston A, Coles A. Multiple sclerosis. Lancet 2002; 359: 1221-1231.

[2] Multiple Sclerosis Society of Canada. Estimated number of Canadians with multiple sclerosis re-examined. Multiple Sclerosis Society of Canada; 2006.

[3] Frohman EM, Racke MK, Raine CS. Multiple sclerosis--the plaque and its pathogenesis. N Engl J Med 2006; 354: 942-955.

[4] Sospedra M, Martin R. Immunology of multiple sclerosis. Annu Rev Immunol 2005; 23: 683-747.

[5] Noseworthy JH, Lucchinetti C, Rodriguez M, Weinshenker BG. Multiple sclerosis. N Engl J Med 2000; 343: 938-952.

[6] Lublin FD, Reingold SC. Defining the clinical course of multiple sclerosis: results of an international survey. National Multiple Sclerosis Society (USA) Advisory Committee on Clinical Trials of New Agents in Multiple Sclerosis. Neurology 1996; 46: 907-911.

[7] Weinshenker BG, Bass B, Rice GP, Noseworthy J, Carriere W, Baskerville J et al. The natural history of multiple sclerosis: a geographically based study. I. Clinical course and disability. Brain 1989; 112 (Pt 1): 133-146.

[8] Compston A, McAlpine D, Confavreux C, Lassmann H, McDonald I. McAlpine's multiple sclerosis. Sydney ; Edinburgh ; New York: Elsevier/Churchill Livingstone; 2005. pp. 201, 347-349.

[9] Heard RN. The spectrum of multiple sclerosis. Curr Allergy Asthma Rep 2007; 7: 280-284.

[10] Calabresi PA. Diagnosis and management of multiple sclerosis. Am Fam Physician 2004; 70: 1935-1944.

[11] McAlpine D, Lumsden C, Acheson E. Multiple sclerosis: a reappraisal. Edinburgh, London: Churchill Livingston; 1972. pp. 135-148.

[12] Olek MJ. Differential diagnosis, clinical features, and prognosis of multiple sclerosis. In: Olek MJ (ed). Multiple sclerosis: etiology, diagnosis, and new treatment strategies. Totowa: Humana Press; 2005. pp. 16, 21-31.

[13] Soderstrom M. Optic neuritis and multiple sclerosis. Acta Ophthalmol Scand 2001; 79: 223-227.

[14] Atlas SW. Magnetic resonance imaging of the brain and spine. New York: Raven Press; 1991. pp. 709-794.

[15] Newman NM. Neuro-ophthalmology : a practical text. Norwalk, Conn.: Appleton & Lange; 1992. pp. 58, 126.

[16] Hickman SJ, Dalton CM, Miller DH, Plant GT. Management of acute optic neuritis. Lancet 2002; 360: 1953-1962.

[17] Beck RW, Cleary PA, Anderson MM, Jr., Keltner JL, Shults WT, Kaufman DI et al. A randomized, controlled trial of corticosteroids in the treatment of acute optic neuritis. The Optic Neuritis Study Group. N Engl J Med 1992; 326: 581-588.

[18] Ghezzi A, Martinelli V, Torri V, Zaffaroni M, Rodegher M, Comi G et al. Long-term follow-up of isolated optic neuritis: the risk of developing multiple sclerosis, its outcome, and the prognostic role of paraclinical tests. J Neurol 1999; 246: 770-775.

[19] Acheson J. Optic nerve and chiasmal disease. J Neurol 2000; 247: 587-596.

[20] McDonald WI, Compston A, Edan G, Goodkin D, Hartung HP, Lublin FD et al. Recommended diagnostic criteria for multiple sclerosis: guidelines from the International Panel on the diagnosis of multiple sclerosis. Ann Neurol 2001; 50: 121-127.

[21] Cole SR, Beck RW, Moke PS, Kaufman DI, Tourtellotte WW. The predictive value of CSF oligoclonal banding for MS 5 years after optic neuritis. Optic Neuritis Study Group. Neurology 1998; 51: 885-887.

[22] Halliday AM, McDonald WI, Mushin J. Visual evoked response in diagnosis of multiple sclerosis. Br Med J 1973; 4: 661-664.

[23] Hume AL, Waxman SG. Evoked potentials in suspected multiple sclerosis: diagnostic value and prediction of clinical course. J Neurol Sci 1988; 83: 191-210.

[24] Altenmuller E, Ruether K, Dichgans I. VEP bei demyelinisierenden Erkrankungen des ZNS. Evozierte Potentiale. Berlin: Spinger; 1990.

[25] Martin M, Hiltner TD, Wood JC, Fraser SE, Jacobs RE, Readhead C. Myelin deficiencies visualized in vivo: visually evoked potentials and T2-weighted magnetic resonance images of shiverer mutant and wild-type mice. J Neurosci Res 2006; 84: 1716-1726.

[26] Martin R, McFarland HF, McFarlin DE. Immunological aspects of demyelinating diseases. Annu Rev Immunol 1992; 10: 153-187.

[27] McFarland HF, Martin R. Multiple sclerosis: a complicated picture of autoimmunity. Nat Immunol 2007; 8: 913-919.

[28] Bar-Or A. The immunology of multiple sclerosis. Semin Neurol 2008; 28: 29-45.

[29] Hohlfeld R. Biotechnological agents for the immunotherapy of multiple sclerosis. Principles, problems and perspectives. Brain 1997; 120 (Pt 5): 865-916.

[30] Haines JL, Terwedow HA, Burgess K, Pericak-Vance MA, Rimmler JB, Martin ER et al. Linkage of the MHC to familial multiple sclerosis suggests genetic heterogeneity. The Multiple Sclerosis Genetics Group. Hum Mol Genet 1998; 7: 1229-1234.

[31] Hillert J, Olerup O. HLA and MS. Neurology 1993; 43: 2426-2427.

[32] Ramagopalan SV, Knight JC, Ebers GC. Multiple sclerosis and the major histocompatibility complex. Curr Opin Neurol 2009; 22: 219-225.

[33] Jersild C, Fog T, Hansen GS, Thomsen M, Svejgaard A, Dupont B. Histocompatibility determinants in multiple sclerosis, with special reference to clinical course. Lancet 1973; 2: 1221-1225.

[34] Terasaki PI, Park MS, Opelz G, Ting A. Multiple sclerosis and high incidence of a B lymphocyte antigen. Science 1976; 193: 1245-1247.

[35] Winchester R, Ebers G, Fu SM, Espinosa L, Zabriskie J, Kunkel HG. B-cell alloantigen Ag 7a in multiple sclerosis. Lancet 1975; 2: 814.

[36] Booth DR, Arthur AT, Teutsch SM, Bye C, Rubio J, Armati PJ et al. Gene expression and genotyping studies implicate the interleukin 7 receptor in the pathogenesis of primary progressive multiple sclerosis. J Mol Med 2005; 83: 822-830.

[37] Zhang Z, Duvefelt K, Svensson F, Masterman T, Jonasdottir G, Salter H et al. Two genes encoding immune-regulatory molecules (LAG3 and IL7R) confer susceptibility to multiple sclerosis. Genes Immun 2005; 6: 145-152.

[38] Hafler DA, Compston A, Sawcer S, Lander ES, Daly MJ, De Jager PL et al. Risk alleles for multiple sclerosis identified by a genomewide study. N Engl J Med 2007; 357: 851-862.

[39] Aulchenko YS, Hoppenbrouwers IA, Ramagopalan SV, Broer L, Jafari N, Hillert J et al. Genetic variation in the KIF1B locus influences susceptibility to multiple sclerosis. Nat Genet 2008; 40: 1402-1403.

[40] Hayes CE. Vitamin D: a natural inhibitor of multiple sclerosis. Proc Nutr Soc 2000; 59: 531-535.

[41] Wucherpfennig KW, Strominger JL. Molecular mimicry in T cell-mediated autoimmunity: viral peptides activate human T cell clones specific for myelin basic protein. Cell 1995; 80: 695-705.

[42] Sriram S, Mitchell W, Stratton C. Multiple sclerosis associated with Chlamydia pneumoniae infection of the CNS. Neurology 1998; 50: 571-572.

[43] Sriram S, Stratton CW, Yao S, Tharp A, Ding L, Bannan JD et al. Chlamydia pneumoniae infection of the central nervous system in multiple sclerosis. Ann Neurol 1999; 46: 6-14.

[44] Tough DF, Sprent J. Viruses and T cell turnover: evidence for bystander proliferation. Immunol Rev 1996; 150: 129-142.

[45] Brocke S, Gaur A, Piercy C, Gautam A, Gijbels K, Fathman CG et al. Induction of relapsing paralysis in experimental autoimmune encephalomyelitis by bacterial superantigen. Nature 1993; 365: 642-644.

[46] Waldner H, Collins M, Kuchroo VK. Activation of antigen-presenting cells by microbial products breaks self tolerance and induces autoimmune disease. J Clin Invest 2004; 113: 990-997.

[47] Fujinami RS, von Herrath MG, Christen U, Whitton JL. Molecular mimicry, bystander activation, or viral persistence: infections and autoimmune disease. Clin Microbiol Rev 2006; 19: 80-94.

[48] Bar-Or A. Immunology of multiple sclerosis. Neurol Clin 2005; 23: 149-175.

[49] Engelhardt B. Molecular mechanisms involved in T cell migration across the blood-brain barrier. J Neural Transm 2006; 113: 477-485.

[50] Agrawal S, Anderson P, Durbeej M, van Rooijen N, Ivars F, Opdenakker G et al. Dystroglycan is selectively cleaved at the parenchymal basement membrane at sites of leukocyte extravasation in experimental autoimmune encephalomyelitis. J Exp Med 2006; 203: 1007-1019.

[51] Steinman L. Multiple sclerosis: a coordinated immunological attack against myelin in the central nervous system. Cell 1996; 85: 299-302.

[52] Steinman L, Waisman A, Altmann D. Major T-cell responses in multiple sclerosis. Mol Med Today 1995; 1: 79-83.

[53] Dhib-Jalbut S. Mechanisms of action of interferons and glatiramer acetate in multiple sclerosis. Neurology 2002; 58: S3-9.

[54] Huseby ES, Liggitt D, Brabb T, Schnabel B, Ohlen C, Goverman J. A pathogenic role for myelin-specific CD8(+) T cells in a model for multiple sclerosis. J Exp Med 2001; 194: 669-676.

[55] Nikbin B, Bonab MM, Khosravi F, Talebian F. Role of B cells in pathogenesis of multiple sclerosis. Int Rev Neurobiol 2007; 79: 13-42.

[56] Zamvil SS, Steinman L. The T lymphocyte in experimental allergic encephalomyelitis. Annu Rev Immunol 1990; 8: 579-621.

[57] Baker D, Jackson S. Models of Multiple Sclerosis. ACNR 2007; 6: 10-12.

[58] Duncan ID, Lunn KF, Holmgren B, Urba-Holmgren R, Brignolo-Holmes L. The taiep rat: a myelin mutant with an associated oligodendrocyte microtubular defect. J Neurocytol 1992; 21: 870-884.

[59] Holmgren B, Urba-Holmgren R, Riboni L, Vega-SaenzdeMiera EC. Sprague Dawley rat mutant with tremor, ataxia, tonic immobility episodes, epilepsy and paralysis. Lab Anim Sci 1989; 39: 226-228.

[60] Privat A, Jacque C, Bourre JM, Dupouey P, Baumann N. Absence of the major dense line in myelin of the mutant mouse "shiverer". Neurosci Lett 1979; 12: 107-112.

[61] Fanarraga ML, Griffiths IR, McCulloch MC, Barrie JA, Kennedy PG, Brophy PJ. Rumpshaker: an X-linked mutation causing hypomyelination: developmental differences in myelination and glial cells between the optic nerve and spinal cord. Glia 1992; 5: 161-170.

[62] Nave KA, Lai C, Bloom FE, Milner RJ. Jimpy mutant mouse: a 74-base deletion in the mRNA for myelin proteolipid protein and evidence for a primary defect in RNA splicing. Proc Natl Acad Sci U S A 1986; 83: 9264-9268.

[63] Biffiger K, Bartsch S, Montag D, Aguzzi A, Schachner M, Bartsch U. Severe hypomyelination of the murine CNS in the absence of myelin-associated glycoprotein and fyn tyrosine kinase. J Neurosci 2000; 20: 7430-7437.

[64] Hall SM. The effect of injections of lysophosphatidyl choline into white matter of the adult mouse spinal cord. J Cell Sci 1972; 10: 535-546.

[65] Matsushima GK, Morell P. The neurotoxicant, cuprizone, as a model to study demyelination and remyelination in the central nervous system. Brain Pathol 2001; 11: 107-116.

[66] Yajima K, Suzuki K. Demyelination and remyelination in the rat central nervous system following ethidium bromide injection. Lab Invest 1979; 41: 385-392.

[67] Rodriguez M, Oleszak E, Leibowitz J. Theiler's murine encephalomyelitis: a model of demyelination and persistence of virus. Crit Rev Immunol 1987; 7: 325-365.

[68] Suckling AJ, Pathak S, Jagelman S, Webb HE. Virus-associated demyelination. A model using avirulent Semliki Forest virus infection of mice. J Neurol Sci 1978; 39: 147-154.

[69] Kuerten S, Angelov DN. Comparing the CNS morphology and immunobiology of different EAE models in C57BL/6 mice - a step towards understanding the complexity of multiple sclerosis. Ann Anat 2008; 190: 1-15.

[70] Steinman L. Optic neuritis, a new variant of experimental encephalomyelitis, a durable model for all seasons, now in its seventieth year. J Exp Med 2003; 197: 1065-1071.

[71] Fritz RB, McFarlin DE. Encephalitogenic epitopes of myelin basic protein. Chem Immunol 1989; 46: 101-125.

[72] Fritz RB, Skeen MJ, Chou CH, Garcia M, Egorov IK. Major histocompatibility complex-linked control of the murine immune response to myelin basic protein. J Immunol 1985; 134: 2328-2332.

[73] Bettelli E. Building different mouse models for human MS. Ann N Y Acad Sci 2007; 1103: 11-18.

[74] Zamvil SS, Mitchell DJ, Moore AC, Kitamura K, Steinman L, Rothbard JB. T-cell epitope of the autoantigen myelin basic protein that induces encephalomyelitis. Nature 1986; 324: 258-260.

[75] Tuohy VK, Lu Z, Sobel RA, Laursen RA, Lees MB. Identification of an encephalitogenic determinant of myelin proteolipid protein for SJL mice. J Immunol 1989; 142: 1523-1527.

[76] Greer JM, Kuchroo VK, Sobel RA, Lees MB. Identification and characterization of a second encephalitogenic determinant of myelin proteolipid protein (residues 178-191) for SJL mice. J Immunol 1992; 149: 783-788.

[77] Greer JM, Sobel RA, Sette A, Southwood S, Lees MB, Kuchroo VK. Immunogenic and encephalitogenic epitope clusters of myelin proteolipid protein. J Immunol 1996; 156: 371-379.

[78] Mendel I, Kerlero de Rosbo N, Ben-Nun A. A myelin oligodendrocyte glycoprotein peptide induces typical chronic experimental autoimmune encephalomyelitis in H-2b mice: fine specificity and T cell receptor V beta expression of encephalitogenic T cells. Eur J Immunol 1995; 25: 1951-1959.

[79] Morris-Downes MM, McCormack K, Baker D, Sivaprasad D, Natkunarajah J, Amor S. Encephalitogenic and immunogenic potential of myelin-associated glycoprotein (MAG), oligodendrocyte-specific glycoprotein (OSP) and 2',3'-cyclic nucleotide 3'-phosphodiesterase (CNPase) in ABH and SJL mice. J Neuroimmunol 2002; 122: 20-33.

[80] Weerth S, Berger T, Lassmann H, Linington C. Encephalitogenic and neuritogenic T cell responses to the myelin-associated glycoprotein (MAG) in the Lewis rat. J Neuroimmunol 1999; 95: 157-164.

[81] Kojima K, Berger T, Lassmann H, Hinze-Selch D, Zhang Y, Gehrmann J et al. Experimental autoimmune panencephalitis and uveoretinitis transferred to the Lewis rat by T lymphocytes specific for the S100 beta molecule, a calcium binding protein of astroglia. J Exp Med 1994; 180: 817-829.

[82] Linington C, Izumo S, Suzuki M, Uyemura K, Meyermann R, Wekerle H. A permanent rat T cell line that mediates experimental allergic neuritis in the Lewis rat in vivo. J Immunol 1984; 133: 1946-1950.

[83] Gardinier MV, Amiguet P, Linington C, Matthieu JM. Myelin/oligodendrocyte glycoprotein is a unique member of the immunoglobulin superfamily. J Neurosci Res 1992; 33: 177-187.

[84] Brunner C, Lassmann H, Waehneldt TV, Matthieu JM, Linington C. Differential ultrastructural localization of myelin basic protein, myelin/oligodendroglial glycoprotein, and 2',3'-cyclic nucleotide 3'-phosphodiesterase in the CNS of adult rats. J Neurochem 1989; 52: 296-304.

[85] Scolding NJ, Frith S, Linington C, Morgan BP, Campbell AK, Compston DA. Myelin-oligodendrocyte glycoprotein (MOG) is a surface marker of oligodendrocyte maturation. J Neuroimmunol 1989; 22: 169-176.

[86] Amiguet P, Gardinier MV, Zanetta JP, Matthieu JM. Purification and partial structural and functional characterization of mouse myelin/oligodendrocyte glycoprotein. J Neurochem 1992; 58: 1676-1682.

[87] Bettelli E, Pagany M, Weiner HL, Linington C, Sobel RA, Kuchroo VK. Myelin oligodendrocyte glycoprotein-specific T cell receptor transgenic mice develop spontaneous autoimmune optic neuritis. J Exp Med 2003; 197: 1073-1081.

[88] Oliver AR, Lyon GM, Ruddle NH. Rat and human myelin oligodendrocyte glycoproteins induce experimental autoimmune encephalomyelitis by different mechanisms in C57BL/6 mice. J Immunol 2003; 171: 462-468.

[89] Hjelmstrom P, Juedes AE, Fjell J, Ruddle NH. B-cell-deficient mice develop experimental allergic encephalomyelitis with demyelination after myelin oligodendrocyte glycoprotein sensitization. J Immunol 1998; 161: 4480-4483.

[90] Berger A. Th1 and Th2 responses: what are they? BMJ 2000; 321: 424.

[91] Freund J. Some aspects of active immunization. Annu Rev Microbiol 1947; 1: 291-308.

[92] Freund J. The mode of action of immunologic adjuvants. In: Birkhäuser H (ed). Advances in tuberculousis research. Basel, Switzerland: Karger; 1956. pp. 130-148.

[93] Freund J, McDermott K. Sensitisation to horse serum by means of adjuvants. Proceedings of the Society of Experimental Biology and Medicine 1942; 49: 548-553.

[94] Al-Omaishi J, Bashir R, Gendelman HE. The cellular immunology of multiple sclerosis. J Leukoc Biol 1999; 65: 444-452.

[95] Segal BM, Chang JT, Shevach EM. CpG oligonucleotides are potent adjuvants for the activation of autoreactive encephalitogenic T cells in vivo. J Immunol 2000; 164: 5683-5688.

[96] Seder RA, Gazzinelli R, Sher A, Paul WE. Interleukin 12 acts directly on CD4+ T cells to enhance priming for interferon gamma production and diminishes interleukin 4 inhibition of such priming. Proc Natl Acad Sci U S A 1993; 90: 10188-10192.

[97] Brocke S, Gijbels K, Steinman L. Experimental autoimmune encephalomyelitis in the mouse. In: Cohen R, Miller A (eds). Autoimmune Disease Models. San Diego: Academic Press; 1994. pp. 1-14.

[98] Munoz JJ, Peacock MG. Action of pertussigen (pertussis toxin) on serum IgE and on Fc epsilon receptors on lymphocytes. Cell Immunol 1990; 127: 327-336.

[99] Sewell WA, de Moerloose PA, Hamilton JA, Schrader JW, Mackay IR, Vadas MA. Potentiation of delayed-type hypersensitivity by pertussigen or cyclophosphamide with release of different lymphokines. Immunology 1987; 61: 483-488.

[100] Lobet Y, Feron C, Dequesne G, Simoen E, Hauser P, Locht C. Site-specific alterations in the B oligomer that affect receptor-binding activities and mitogenicity of pertussis toxin. J Exp Med 1993; 177: 79-87.

[101] Ryan M, McCarthy L, Rappuoli R, Mahon BP, Mills KH. Pertussis toxin potentiates Th1 and Th2 responses to co-injected antigen: adjuvant action is associated with enhanced regulatory cytokine production and expression of the co-stimulatory molecules B7-1, B7-2 and CD28. Int Immunol 1998; 10: 651-662.

[102] Rabchevsky AG, Degos JD, Dreyfus PA. Peripheral injections of Freund's adjuvant in mice provoke leakage of serum proteins through the blood-brain barrier without inducing reactive gliosis. Brain Res 1999; 832: 84-96.

[103] Shive CL, Hofstetter H, Arredondo L, Shaw C, Forsthuber TG. The enhanced antigen-specific production of cytokines induced by pertussis toxin is due to clonal expansion of T cells and not to altered effector functions of long-term memory cells. Eur J Immunol 2000; 30: 2422-2431.

[104] Lyons JA, San M, Happ MP, Cross AH. B cells are critical to induction of experimental allergic encephalomyelitis by protein but not by a short encephalitogenic peptide. Eur J Immunol 1999; 29: 3432-3439.

[105] Chitnis T. The role of CD4 T cells in the pathogenesis of multiple sclerosis. Int Rev Neurobiol 2007; 79: 43-72.

[106] Lassmann H, Wisniewski HM. Chronic relapsing experimental allergic encephalomyelitis: clinicopathological comparison with multiple sclerosis. Arch Neurol 1979; 36: 490-497.

[107] Tafreshi AP, Mostafavi H, Zeynali B. Induction of experimental allergic encephalomyelitis in C57/BL6 Mice: an animal model for multiple sclerosis. Iran J Allergy Asthma Immunol 2005; 4: 113-117.

[108] Slavin A, Ewing C, Liu J, Ichikawa M, Slavin J, Bernard CC. Induction of a multiple sclerosis-like disease in mice with an immunodominant epitope of myelin oligodendrocyte glycoprotein. Autoimmunity 1998; 28: 109-120.

[109] Day MJ. Histopathology of EAE. In: Lavi E, Constantinescu CS (eds). Experimental Models of Multiple Sclerosis. New York: Springer Science; 2005. pp. 25-43.

[110] Pivneva T, Kolotoushkina E, Mel'nik N. Mechanisms of the demyelination process and its modelling. Neurophysiology 1999; 31: 403-412.

[111] Wang D, Ayers MM, Catmull DV, Hazelwood LJ, Bernard CC, Orian JM. Astrocyte-associated axonal damage in pre-onset stages of experimental autoimmune encephalomyelitis. Glia 2005; 51: 235-240.

[112] Wu Q, Butzkueven H, Gresle M, Kirchhoff F, Friedhuber A, Yang Q et al. MR diffusion changes correlate with ultra-structurally defined axonal degeneration in murine optic nerve. Neuroimage 2007; 37: 1138-1147.

[113] Pettinelli CB, McFarlin DE. Adoptive transfer of experimental allergic encephalomyelitis in SJL/J mice after in vitro activation of lymph node cells by myelin basic protein: requirement for Lyt 1+ 2- T lymphocytes. J Immunol 1981; 127: 1420-1423.

[114] Kuchroo VK, Martin CA, Greer JM, Ju ST, Sobel RA, Dorf ME. Cytokines and adhesion molecules contribute to the ability of myelin proteolipid protein-specific

T cell clones to mediate experimental allergic encephalomyelitis. J Immunol 1993; 151: 4371-4382.

[115] Langrish CL, Chen Y, Blumenschein WM, Mattson J, Basham B, Sedgwick JD et al. IL-23 drives a pathogenic T cell population that induces autoimmune inflammation. J Exp Med 2005; 201: 233-240.

[116] Aloisi F, Serafini B, Adorini L. Glia-T cell dialogue. J Neuroimmunol 2000; 107: 111-117.

[117] Lyons JA, Ramsbottom MJ, Cross AH. Critical role of antigen-specific antibody in experimental autoimmune encephalomyelitis induced by recombinant myelin oligodendrocyte glycoprotein. Eur J Immunol 2002; 32: 1905-1913.

[118] Spahn TW, Issazadah S, Salvin AJ, Weiner HL. Decreased severity of myelin oligodendrocyte glycoprotein peptide 33 - 35-induced experimental autoimmune encephalomyelitis in mice with a disrupted TCR delta chain gene. Eur J Immunol 1999; 29: 4060-4071.

[119] Ayers M, Hazelwood L, Catmull D, Wang D, McKormack Q, Bernard C et al. Early glial responses in murine models of multiple sclerosis. Neurochemistry International 2004; 45: 409-419.

[120] Polman CH, Reingold SC, Edan G, Filippi M, Hartung HP, Kappos L et al. Diagnostic criteria for multiple sclerosis: 2005 revisions to the "McDonald Criteria". Ann Neurol 2005; 58: 840-846.

[121] Li DK, Li MJ, Traboulsee A, Zhao G, Riddehough A, Paty D. The use of MRI as an outcome measure in clinical trials. Adv Neurol 2006; 98: 203-226.

[122] Bloch F. Nuclear Induction. Physical Review 1946; 70: 460-474.

[123] Horsefield M. Basis of MRI Contrast. In: Filippi M, Nicola S, Dousset V, McGowan J (eds). MR Imaging in White Matter Diseases of the Brain and Spinal Cord. Berlin, Heidelberg: Springer-Verlag Berlin Heidelberg; 2005. pp. 3-12.

[124] Bushberg JT, Siebert JA, Leidholdt JR EM, Boone JM. The essential physics of medical imaging. Philadelphia: Lippincott Williams & Wilkins; 2002. pp. 373-442.

[125] Callaghan PT. Principles of nuclear magnetic resonance microscopy. Oxford science publications. Oxford [England] ; New York: Oxford University Press; 1991. pp. 30, 38.

[126] Hashemi RH, Bradley WG, Lisanti CJ. Philadelphia: Lippincott Williams & Wilkins; 2004.

[127] Guilfoyle DN, Dyakin VV, O'Shea J, Pell GS, Helpern JA. Quantitative measurements of proton spin-lattice (T1) and spin-spin (T2) relaxation times in the mouse brain at 7.0 T. Magn Reson Med 2003; 49: 576-580.

[128] Pirko I, Fricke ST, Johnson AJ, Rodriguez M, Macura SI. Magnetic resonance imaging, microscopy, and spectroscopy of the central nervous system in experimental animals. NeuroRx 2005; 2: 250-264.

[129] Miller DH, McDonald WI. Neuroimaging in multiple sclerosis. Clin Neurosci 1994; 2: 215-224.

[130] Bruck W, Bitsch A, Kolenda H, Bruck Y, Stiefel M, Lassmann H. Inflammatory central nervous system demyelination: correlation of magnetic resonance imaging findings with lesion pathology. Ann Neurol 1997; 42: 783-793.

[131] McDonald WI, Barnes D. Lessons from magnetic resonance imaging in multiple sclerosis. Trends Neurosci 1989; 12: 376-379.

[132] McDonald WI, Miller DH, Barnes D. The pathological evolution of multiple sclerosis. Neuropathol Appl Neurobiol 1992; 18: 319-334.

[133] van Waesberghe JH, Kamphorst W, De Groot CJ, van Walderveen MA, Castelijns JA, Ravid R et al. Axonal loss in multiple sclerosis lesions: magnetic resonance imaging insights into substrates of disability. Ann Neurol 1999; 46: 747-754.

[134] Nessler S, Boretius S, Stadelmann C, Bittner A, Merkler D, Hartung HP et al. Early MRI changes in a mouse model of multiple sclerosis are predictive of severe inflammatory tissue damage. Brain 2007; 130: 2186-2198.

[135] Barkhof F. The clinico-radiological paradox in multiple sclerosis revisited. Curr Opin Neurol 2002; 15: 239-245.

[136] Zivadinov R, Leist TP. Clinical-magnetic resonance imaging correlations in multiple sclerosis. J Neuroimaging 2005; 15: 10S-21S.

[137] Miller DH. Magnetic resonance in monitoring the treatment of multiple sclerosis. Ann Neurol 1994; 36 Suppl: S91-94.

[138] Filippi M, Paty DW, Kappos L, Barkhof F, Compston DA, Thompson AJ et al. Correlations between changes in disability and T2-weighted brain MRI activity in multiple sclerosis: a follow-up study. Neurology 1995; 45: 255-260.

[139] Rovaris M, Gass A, Bammer R, Hickman SJ, Ciccarelli O, Miller DH et al. Diffusion MRI in multiple sclerosis. Neurology 2005; 65: 1526-1532.

[140] Filippi M, Cercignani M, Inglese M, Horsfield MA, Comi G. Diffusion tensor magnetic resonance imaging in multiple sclerosis. Neurology 2001; 56: 304-311.

[141] Goldberg-Zimring D, Mewes AU, Maddah M, Warfield SK. Diffusion tensor magnetic resonance imaging in multiple sclerosis. J Neuroimaging 2005; 15: 68S-81S.

[142] Filippi M, Inglese M. Overview of diffusion-weighted magnetic resonance studies in multiple sclerosis. J Neurol Sci 2001; 186 Suppl 1: S37-43.

[143] Horsfield MA. Using diffusion-weighted MRI in multicenter clinical trials for multiple sclerosis. J Neurol Sci 2001; 186 Suppl 1: S51-54.

[144] Horsfield MA, Jones DK. Applications of diffusion-weighted and diffusion tensor MRI to white matter diseases - a review. NMR Biomed 2002; 15: 570-577.

[145] Rovaris M, Filippi M. MR-based technology for in vivo detection, characterization, and quantification of pathology of relapsing-remitting multiple sclerosis. J Rehabil Res Dev 2002; 39: 243-259.

[146] Einstein A. Investigations on the theory of the Brownian movement. New York: Dover Publications; 1956.

[147] Bernstein MA, King KF, Zhou ZJ. Advanced pulse sequence techniques: diffusion imaging. Handbook of MRI pulse sequences. Amsterdam ; Boston: Elsevier Academic Press; 2004. pp. 830-856.

[148] Tanner JE. Transient diffusion in a system partitioned by permeable barriers. Application to NMR measurements with a pulsed field gradient. J Chem Phys 1978; 69: 1748-1754.

[149] Le Bihan D, Breton E, Lallemand D, Grenier P, Cabanis E, Laval-Jeantet M. MR imaging of intravoxel incoherent motions: application to diffusion and perfusion in neurologic disorders. Radiology 1986; 161: 401-407.

[150] Finch ED, Harmon JF, Muller BH. Pulsed NMR measurements of the diffusion constant of water in muscle. Arch Biochem Biophys 1971; 147: 299-310.

[151] Hansen JR. Pulsed NMR study of water mobility in muscle and brain tissue. Biochim Biophys Acta 1971; 230: 482-486.

[152] Jones DK. Fundamentals of diffusion mr imaging. In: Gillard J, Waldman A, Barker P (eds). Clinical mr neuroimaging: diffusion, perfusion, spectroscopy. Cambridge, UK: Cambridge University Press London; 2005. pp. 54-85.

[153] Stejskal E, Tanner J. Spin diffusion measurements: spin echoes in the presence of a time-dependent field gradient. J Chem Phys 1965; 42: 288-292.

[154] Song SK, Sun SW, Ramsbottom MJ, Chang C, Russell J, Cross AH. Dysmyelination revealed through MRI as increased radial (but unchanged axial) diffusion of water. Neuroimage 2002; 17: 1429-1436.

[155] Song SK, Yoshino J, Le TQ, Lin SJ, Sun SW, Cross AH et al. Demyelination increases radial diffusivity in corpus callosum of mouse brain. Neuroimage 2005; 26: 132-140.

[156] Sun SW, Liang HF, Trinkaus K, Cross AH, Armstrong RC, Song SK. Noninvasive detection of cuprizone induced axonal damage and demyelination in the mouse corpus callosum. Magn Reson Med 2006; 55: 302-308.

[157] Nair G, Tanahashi Y, Low HP, Billings-Gagliardi S, Schwartz WJ, Duong TQ. Myelination and long diffusion times alter diffusion-tensor-imaging contrast in myelin-deficient shiverer mice. Neuroimage 2005; 28: 165-174.

[158] Pierpaoli C, Barnett A, Pajevic S, Chen R, Penix LR, Virta A et al. Water diffusion changes in Wallerian degeneration and their dependence on white matter architecture. Neuroimage 2001; 13: 1174-1185.

[159] Song SK, Sun SW, Ju WK, Lin SJ, Cross AH, Neufeld AH. Diffusion tensor imaging detects and differentiates axon and myelin degeneration in mouse optic nerve after retinal ischemia. Neuroimage 2003; 20: 1714-1722.

[160] Sun SW, Liang HF, Schmidt RE, Cross AH, Song SK. Selective vulnerability of cerebral white matter in a murine model of multiple sclerosis detected using diffusion tensor imaging. Neurobiol Dis 2007; 28: 30-38.

[161] Moseley ME, Cohen Y, Kucharczyk J, Mintorovitch J, Asgari HS, Wendland MF et al. Diffusion-weighted MR imaging of anisotropic water diffusion in cat central nervous system. Radiology 1990; 176: 439-445.

[162] Beaulieu C. The basis of anisotropic water diffusion in the nervous system - a technical review. NMR Biomed 2002; 15: 435-455.

[163] Werring DJ, Clark CA, Barker GJ, Thompson AJ, Miller DH. Diffusion tensor imaging of lesions and normal-appearing white matter in multiple sclerosis. Neurology 1999; 52: 1626-1632.

[164] Xu J, Sun SW, Naismith RT, Snyder AZ, Cross AH, Song SK. Assessing optic nerve pathology with diffusion MRI: from mouse to human. NMR Biomed 2008; 21: 928-940.

[165] Ebisu T, Naruse S, Horikawa Y, Ueda S, Tanaka C, Uto M et al. Discrimination between different types of white matter edema with diffusion-weighted MR imaging. J Magn Reson Imaging 1993; 3: 863-868.

[166] Sotak CH. The role of diffusion tensor imaging in the evaluation of ischemic brain injury - a review. NMR Biomed 2002; 15: 561-569.

[167] Zelaya F, Flood N, Chalk JB, Wang D, Doddrell DM, Strugnell W et al. An evaluation of the time dependence of the anisotropy of the water diffusion tensor in acute human ischemia. Magn Reson Imaging 1999; 17: 331-348.

[168] Beaulieu C, Allen PS. Water diffusion in the giant axon of the squid: implications for diffusion-weighted MRI of the nervous system. Magn Reson Med 1994; 32: 579-583.

[169] Beaulieu C, Does MD, Snyder RE, Allen PS. Changes in water diffusion due to Wallerian degeneration in peripheral nerve. Magn Reson Med 1996; 36: 627-631.

[170] Ford JC, Hackney DB, Alsop DC, Jara H, Joseph PM, Hand CM et al. MRI characterization of diffusion coefficients in a rat spinal cord injury model. Magn Reson Med 1994; 31: 488-494.

[171] Schneider JT, Faber C. BOLD imaging in the mouse brain using a turboCRAZED sequence at high magnetic fields. Magn Reson Med 2008; 60: 850-859.

[172] Kangarlu A. Molecular imaging and high-field MRI in multiple sclerosis. In: Filippi M, Dousset V, McGowan JC, Stefano N, SpringerLink (Online service) (eds). MR Imaging in White Matter Diseases of the Brain and Spinal Cord. Berlin, Heidelberg: Springer-Verlag Berlin Heidelberg; 2005. pp. 129-148.

[173] Pirko I, Johnson AJ. Neuroimaging of demyelination and remyelination models. Curr Top Microbiol Immunol 2008; 318: 241-266.

[174] Schellenberg AE, Buist R, Yong VW, Del Bigio MR, Peeling J. Magnetic resonance imaging of blood-spinal cord barrier disruption in mice with experimental autoimmune encephalomyelitis. Magn Reson Med 2007; 58: 298-305.

[175] Tsutsui S, Schnermann J, Noorbakhsh F, Henry S, Yong VW, Winston BW et al. A1 adenosine receptor upregulation and activation attenuates neuroinflammation and demyelination in a model of multiple sclerosis. J Neurosci 2004; 24: 1521-1529.

[176] Giuliani F, Fu SA, Metz LM, Yong VW. Effective combination of minocycline and interferon-beta in a model of multiple sclerosis. J Neuroimmunol 2005; 165: 83-91.

[177] Onuki M, Ayers MM, Bernard CC, Orian JM. Axonal degeneration is an early pathological feature in autoimmune-mediated demyelination in mice. Microsc Res Tech 2001; 52: 731-739.

[178] Chavakula V, Martin M, Procissi D, Kim A, Zhang XW, Fraser SE et al. Longitudinal studies of myelin oligodendrocyte glycoprotein-induced EAE using visually evoked potentials and MRI. The 21st Biennial International Society for Neurochemistry – American Society Neurochemistry (ISN – ASN) Joint Meeting. Mexico; 2007.

[179] Giuliani F, Metz LM, Wilson T, Fan Y, Bar-Or A, Yong VW. Additive effect of the combination of glatiramer acetate and minocycline in a model of MS. J Neuroimmunol 2005; 158: 213-221.

[180] Thomas DL, Pell GS, Lythgoe MF, Gadian DG, Ordidge RJ. A quantitative method for fast diffusion imaging using magnetization-prepared TurboFLASH. Magn Reson Med 1998; 39: 950-960.

[181] Franklin KBJ, Paxinos G. The mouse brain in stereotaxic coordinates. New York: Elsevier Academic Press; 2008.

[182] Stromnes IM, Goverman JM. Active induction of experimental allergic encephalomyelitis. Nat Protoc 2006; 1: 1810-1819.

[183] Ben-Chetrit E, Brocke S. Induction of EAE. In: Lavi E, Constantinescu CS (eds). Experimental Models of Multiple Sclerosis. New York: Springer Science; 2005. pp. 11-24.

[184] Lindsey JW. EAE: History, Clinical Signs, and Disease Course. In: Lavi E, Constantinescu CS (eds). Experimental Models of Multiple Sclerosis. New York: Springer Science; 2005. pp. 1-9.

[185] Montgomery IN, Rauch HC. Experimental allergic encephalomyelitis (EAE) in mice: primary control of EAE susceptibility is outside the H-2 complex. J Immunol 1982; 128: 421-425.

[186] Charles River. Weight Chart for the C57BL/6NCrl Mouse. 2008.

[187] Albouz-Abo S, Wilson JC, Bernard CC, von Itzstein M. A conformational study of the human and rat encephalitogenic myelin oligodendrocyte glycoprotein peptides 35-55. Eur J Biochem 1997; 246: 59-70.

[188] Brown DA, Sawchenko PE. Time course and distribution of inflammatory and neurodegenerative events suggest structural bases for the pathogenesis of experimental autoimmune encephalomyelitis. J Comp Neurol 2007; 502: 236-260.

[189] Garthwaite G, Batchelor AM, Goodwin DA, Hewson AK, Leeming K, Ahmed Z et al. Pathological implications of iNOS expression in central white matter: an ex vivo study of optic nerves from rats with experimental allergic encephalomyelitis. Eur J Neurosci 2005; 21: 2127-2135.

[190] Muller DM, Pender MP, Greer JM. A neuropathological analysis of experimental autoimmune encephalomyelitis with predominant brain stem and cerebellar involvement and differences between active and passive induction. Acta Neuropathol 2000; 100: 174-182.

[191] Bernard CC, Johns TG, Slavin A, Ichikawa M, Ewing C, Liu J et al. Myelin oligodendrocyte glycoprotein: a novel candidate autoantigen in multiple sclerosis. J Mol Med 1997; 75: 77-88.

[192] Teuscher C, Bunn JY, Fillmore PD, Butterfield RJ, Zachary JF, Blankenhorn EP. Gender, age, and season at immunization uniquely influence the genetic control of susceptibility to histopathological lesions and clinical signs of experimental allergic encephalomyelitis: implications for the genetics of multiple sclerosis. Am J Pathol 2004; 165: 1593-1602.

[193] Mendel Kerlero de Rosbo N, Ben-Nun A. Delineation of the minimal encephalitogenic epitope within the immunodominant region of myelin oligodendrocyte glycoprotein: diverse V beta gene usage by T cells recognizing

the core epitope encephalitogenic for T cell receptor V beta b and T cell receptor V beta a H-2b mice. Eur J Immunol 1996; 26: 2470-2479.

[194] Tonra JR, Reiseter BS, Kolbeck R, Nagashima K, Robertson R, Keyt B et al. Comparison of the timing of acute blood-brain barrier breakdown to rabbit immunoglobulin G in the cerebellum and spinal cord of mice with experimental autoimmune encephalomyelitis. J Comp Neurol 2001; 430: 131-144.

[195] Ono J, Harada K, Takahashi M, Maeda M, Ikenaka K, Sakurai K et al. Differentiation between dysmyelination and demyelination using magnetic resonance diffusional anisotropy. Brain Res 1995; 671: 141-148.

[196] Thiessen J. Diffusion Tensor Imaging with MRI. Physics. Winnipeg: University of Winnipeg; 2007.

[197] Basser PJ, Jones DK. Diffusion-tensor MRI: theory, experimental design and data analysis - a technical review. NMR Biomed 2002; 15: 456-467.

[198] Holz M, Heil SR, Sacco A. Temperature-dependent self-diffusion coefficients of water and six selected molecular liquids for calibration in accurate 1H NMR PFG measurements. Phys Chem Chem Phys 2000; 2: 4740-4742.

[199] Speedy R, Angell C. Isothermal compressibility of supercooled water and evidence for a thermodynamic singularity at −45°C. J Chem Phys 1976; 65: 851-858.

[200] Colello SJ, Guillery RW. The changing pattern of fibre bundles that pass through the optic chiasm of mice. Eur J Neurosci 1998; 10: 3653-3663.

[201] Neveu MM, Jeffery G. Chiasm formation in man is fundamentally different from that in the mouse. Eye 2007; 21: 1264-1270.

[202] Ono J, Harada K, Sakurai K, Kodaka R, Shimidzu N, Tanaka J et al. MR diffusion imaging in Pelizaeus-Merzbacher disease. Brain Dev 1994; 16: 219-223.

[203] Beaulieu C, Allen PS. Determinants of anisotropic water diffusion in nerves. Magn Reson Med 1994; 31: 394-400.

[204] Richards TL, Alvord EC, Jr., He Y, Petersen K, Peterson J, Cosgrove S et al. Experimental allergic encephalomyelitis in non-human primates: diffusion imaging of acute and chronic brain lesions. Mult Scler 1995; 1: 109-117.

[205] Karlik SJ, Munoz D, St Louis J, Strejan G. Correlation between MRI and clinico-pathological manifestations in Lewis rats protected from experimental allergic encephalomyelitis by acylated synthetic peptide of myelin basic protein. Magn Reson Imaging 1999; 17: 731-737.

[206] Bettelli E, Sullivan B, Szabo SJ, Sobel RA, Glimcher LH, Kuchroo VK. Loss of T-bet, but not STAT1, prevents the development of experimental autoimmune encephalomyelitis. J Exp Med 2004; 200: 79-87.

[207] Delarasse C, Daubas P, Mars LT, Vizler C, Litzenburger T, Iglesias A et al. Myelin/oligodendrocyte glycoprotein-deficient (MOG-deficient) mice reveal lack of immune tolerance to MOG in wild-type mice. J Clin Invest 2003; 112: 544-553.

Appendix A. Experimental log of C57BL/6 mice

Experiment	Date of immunization	$N_{MOG35-55}$	N_{EAE} (%)	$N_{wild\ type}$	N_{sham}
Former 1st	01/17/2007	10 [a]	0 (0)	0	0
1	02/28/2007	10 [b]	7 (70)	0	0
2	06/20/2007	5	4 (80)	1	1
3	07/04/2007	6	0 (0)	1	1
4	09/19/2007	4	0 (0)	1	1
5	10/03/2007	5	4 (80)	1	0
6	10/24/2007	4	3 (75)	2	0
7	11/08/2007	6	5 (83)	0	0
N_{total}		50 [c]	23 (59)	6	3

[a]Mice from the former experiment 1 (N=10) and [b]from experiment 1 (N=1) were removed from the data because of misplaced intraperitoneal injections. These injections might have entered the liver, spleen and seminal vesicle and caused fatalities (N=3) or required humane euthanasia (N=8). Significant (rapid) reduction in body weight, spontaneous rolling and hunched over posture necessitated humane euthanasia (ACC, personal communication, 2008). [c]Following the elimination (N=11), data was analyzed from $N_{MOG35-55} = 50 - 11 = 39$ mice plus $N_{wild\ type} = 6$ and $N_{sham} = 3$. Therefore, N_{total} = total number of mice = 48. $N_{MOG35-55}$ = number of MOG_{35-55}-immunized mice, N_{EAE} = number of EAE mice, $N_{wild\ type}$ = number of wild type control mice and N_{sham} = number of sham control mice. The incidence of EAE per each experiment was added as %. The total incidence of EAE disease was 23/39 (59%).

Appendix B. Mild* EAE induction protocol with MOG_{35-55} peptide

(as provided by the NMR lab) *This protocol only utilized 50 μg of MOG_{35-55}/mouse.

Animal	C57BL/6
Sex	Female
Age	11 weeks old
Reagents	MOG_{35-55}, stock solution 1 mg/ml in PBS (-70°C) CFA H37RA, Fisher #DF 3113-60 (RT) PTX, stock 50 μg/ml in PBS, List Biological Labs 4°C

Basic Protocol:

Day 0	Each mouse gets 2 x 50μl of MOG_{35-55} (subcutaneous injections) near the base of the tail, plus 200 μl of PTX (intraperitoneal injection).
Day 2	Each mouse gets another 200 μl of PTX.
Day 3	Begin daily assessment for bodyweight and for clinical changes (i.e., assess clinical score).

The first sign of disease is often presented by a drop in weight by ~ 1 g.

Scoring:

Tail	1=weak or partially limp tail and 2=fully limp tail
Each limb	1=weakness (unusual gait), 2=dragging limb and 3=full paralysis

Preparation:

- Mild protocol does not require any extra mycobacterium. Use straight CFA.
- Dilute enough stock PTX to 1.5 μg/ml, each mouse gets 0.3 μg/200 μl PBS.
- Only make enough working solution per experiment (activity wears off in a few weeks).
- Mix MOG_{35-55} solution and CFA suspension 1:1 by taking up required volume into glass syringes.
- Attach syringes to a 3-way key, eliminate air bubbles, and mix extremely well.
- Keep chilled on ice when not mixing the solution.

Calculations:

- Each mouse gets 50 μg MOG_{35-55} in 100 μl = 0.5 mg/ml solution BUT this will be mixed 1:1 with CFA so you need to start with twice the working concentration (e.g., 2 ml of 1 mg/ml MOG_{35-55} = 2 mg total MOG_{35-55}, mixed with 2 ml of CFA = 0.5 mg/ml final).
- Inject 100 μl (2 x 50 μl) to deliver 50 μg.
- Allow for at least 200 μl extra to fill the space in the 3-way key.

Appendix C. Monitoring record sheet

(as provided by the NMR lab)

Monitoring Record

Animal ID: Date of Innoculation:

					Detailed Scoring System					Standard Scoring System				
					Hind Limbs		Front Limbs		Total	Score				
Time Point	Date	Time	Weight (g)	Tail	Left	Right	Left	Right	0-14	0-5	Food	Fluids	Initials	Comments
Day														

When a standard score of 1 is observed provide bacon softies. When a standard score of 2 is observed administer 1cc saline subcutaneously.

Standard (old) scoring system:

0=no symptoms

1=limp tail

2=hind limb paresis

3=hind limb paralysis with moderate forelimb weakness

4=quadriplegia or moribund

5=death

Appendix D. NMR monitoring form*

(as provided by the NMR lab)

*In most cases, these specifics were recorded directly to the lab book

Investigator: _____
Animal: _____
Species: _____
Ailment: _____

NMR Date: _____
Anaesthetic: _____

Duration of Anaesthetic: _____
Time Returned to Cage: _____

Time	External Body Temperature (^{o}C)	Respiration Rate (breaths/min)

Comments:

_____
_____
_____
_____
_____
_____

Appendix E. EAE mouse NMRI protocol for DWI

(as provided by the NMR lab)

TURN ON:

- POWER: green button at the bottom of left-most module
- GRADIENTS: on/off/on (red/blue/red) button above power button on the Left-most module
- MEASURE: amber MEAS button on computer
- AIR (if needed): valve to the right of air vent
- VENTILATOR: switch is located at the far end of room (near office)
- RESPIRATORY MONITOR: SAM PC program on laptop
- Login on computer, open ParaVision 2.0.1
    - Single-click PV2.0.1 [RJB]

SET-UP:

- Position coil in holder and secure
- Position respiratory pad and temperature probes on paper towel
- Ensure that anaesthesia is attached to mouse in/out tubes

ENTER NEW PATIENT:

- Enter 8 character NAME and REGISTRATION
    - No punctuation, both must start with a letter
    - Both are necessary to continue
- Enter appropriate comments
- ACCEPT
- LOCATION: EAE
- ENTRY: feet first
- POSITION: prone
- ACCEPT

ANAESTHETIZE MOUSE:

- Turn on gas, adjust proper levels:
    - O_2=200
    - NO_2=300
    - Isoflurane=5
- With mouse in gas chamber, apply anaesthesia for ~ 40 seconds, or until the breathing rate slows down
- Turn on pump and set gas to flow into magnet room
- Race to coil, secure mouse, and position coil in the bore, 55.8 cm away from magnet edge

TUNE RF COIL:

- Open TOOLS
- ACQ: Tune – tune magnet so there are only 3 bars at each setting
- STOP

BEGIN SCANNING:
LOAD SCAN PROTOCOL: MT_flash
Scan 1:1:1 → axial scout scan to find position of mouse in the coil

- Edit IMND: variable attenuator to 30 dB
- Tx0: 18
- Tx1: 9
- RECIEVER GAIN: 500
- GOP

CLONE SCAN 1:1:1
LOAD SCAN PROTOCOL: onepulse → scan used for shimming

- OFFSET: 2000 Hz
- RECEIVER GAIN: 50
  - Decrease gain to ensure that digitizer filling is <100%
- GSP
- TOOLS: shim tool
  - Set sensitivities: 2.0, 1.0, 2.0, 5.0
  - Optimize variables: Y, X, Z, Z^2, XZ, YZ, X^2-Y^2, XY, Y, X, Z
- STOP
- ACQ: auto SF
- DELETE SCAN

CLONE SCAN 1:1:1; MT_flash
Scan 1:2:1 → coronal scout scan used to determine centerline of brain

- GEOMETRY: sagittal
  - Align slice along the centerline of the brain, then add (or subtract) 90°
  - Adjust POSITION, but do not adjust OFFCENTER
- ACCEPT
- GOP

CLONE SCAN 1:2:1; MT_flash
Scan 1:3:1 → sagittal scout scan used to determine slice position of diffusion image

- IMPORT GEOMETRY: 1:2:1
  - Add 90°
- LOAD REFERENCE 1:2:1
  - Align slice along the centerline of the brain
  - Adjust POSITION, but do not adjust OFFCENTER
- ACCEPT
- GOP

CLONE SCAN 1:3:1; MT_flash
Scan 1:4:1 → axial scout scan at position of diffusion image

- LOAD REFERENCE 1:3:1
  - Align slice along the top of the brain – if desired – and add 90°

        - Align slice just above the optic chiasm; (bright spot on bottom of sagittal image)
    - ACCEPT
    - GOP

CLONE SCAN 1:4:1
LOAD SCAN PROTOCOL: MSME_TE_27_Red_BW_quant
Scan 1:5:1 → T2W image

- IMPORT GEOMETRY: 1:4:1
- LOAD REFERENCE: 1:3:1
    - Ensure slice is located on and just above the optic chiasm
    - Adjust POSITION, but do not adjust OFFCENTER
- NUMBER OF SLICES: 1
- SLICE THICKNESS: 0.75 mm
- READOUT: A-P
- FOV: 2.5 cm
    - MOVE SLICES OFFCENTER; ensure that the 1 in the fuchsia box is outside the brain
- ACCEPT
- Edit IMND:
    - VARIABLE ATTENUATOR: 6 dB
    - AVERAGES: 2
    - ECHOS: 8
- RECEIVER GAIN: 150
- Tx0: 23
- Tx1: 14
- GSP: un-shuffle acq-Display
    - Change Tx0 to 17 (23-6), and check to see if signal is close to 0
    - Turn INDEPENDENT SCALES off
    - Adjust Tx0 accordingly; get signal as close to 0 as possible without turning positive → this is the 180 degree pulse
- STOP
- GOP

CLONE SCAN 1:4:1
LOAD SCAN PROTOCOL: flash_dwi_50kHz_4
Scan 1:6:1 → diffusion-weighted imaging in y-direction; gradient applied in phase direction

- IMPORT GEOMETRY: 1:4:1
- SLICE THICKNESS: 1.00 mm
- READOUT: L-R
- FOV: 4.0 cm (thicker for DWI than for T2W)
- ACCEPT
- RECEIVER GAIN: 2000
- Tx0: 18
- Tx1: 14 or value from (1:5:1 + 1.5)

- GOP

CLONE SCAN 1:6:1: flash_dwi_50kHz_4
Scan 1:7:1 → complementary diffusion-weighted image in y-direction; gradient applied in phase direction
- Edit ACQP
  - PULSE PROGRAM: flash_d312.ppg
- GOP

CLONE SCAN 1:6:1: flash_dwi_50kHz_4
Scan 1:8:1 → diffusion-weighted image in x-direction; gradient applied in read direction
- Edit ACQP
  - GRADIENT PROGRAM: flash_dwix
- GOP

CLONE SCAN 1:8:1: flash_dwi_50kHz_4
Scan 1:9:1 → complementary diffusion-weighted image in x-direction; gradient read in phase direction
- Edit ACQP
  - PULSE PROGRAM: flash_d312.ppg
- GOP

CLONE SCAN 1:6:1: flash_dwi_50kHz_4
Scan 1:10:1 → diffusion-weighted image in z-direction; gradient applied in slice direction
- Edit ACQP
  - PULSE PROGRAM: flash_dwislice
- GOP

CLONE SCAN 1:10:1: flash_dwi_50kHz_4
Scan 1:7:1 → complementary diffusion-weighted image in z-direction; gradient applied in slice direction
- Edit ACQP
  - PULSE PROGRAM: flash_d312.ppg
- GOP

TURN OFF:
- VENTILATION (if used)
- AIR (if used)
- MEASURE
- GRADIENTS
- POWER
- SHIMS
- EXIT ParaVision, and logoff computer

Appendix F. Plastic section and electron microscopy (EM) protocol

(as provided by the Department of Pathology at the Health Science Centre)

Once the optic nerve-chiasm specimens were received from mice that were perfused transcardially with 2% glutaraldehyde – 2% paraformaldehyde in phosphate buffer (from which the head was further immersion fixed overnight at 4°C, the brain was removed and the optic chiasm carefully separated and split in the midline to ensure that left-right orientation was not lost), they were post-fixed in 1% osmium tetroxide, dehydrated through graded alcohols, and embedded in epoxy resin. Semi-thin sections (0.5 μm) were stained with toluidine blue for light microscopic examination. Thin sections (80 nm) were mounted on copper grids and contrasted with uranyl acetate-lead citrate for electron microscopic examination (JEOL 1010 microscope).